# Double-Loop Fuzzy Neural Network-Based Fixed-Time Robust Control for Antagonistic PM-Actuated Wrist Robots With Motion Constraints

Yuexuan Xu, Shuzhen Diao, *Graduate Student Member, IEEE*, Tong Yang, *Member, IEEE*, Xinlin Zhang, Ming Li, Yakun Gao, David Navarro-Alarcon, *Senior Member, IEEE*, and Ning Sun, *Senior Member, IEEE*

***Abstract*—Antagonistic pneumatic muscle (PM)-actuated wrist robots have great potential in rehabilitation and industrial applications. The antagonistic connection of PMs, which mimics the agonist-antagonist muscle pairs in human joints, provides substantial advantages such as improved joint stability and a better balance of torque disturbances. However, PM-actuated robots exhibit complex nonlinearities, such as hysteresis, creep, input delay, and time-varying parameters, while also confronting challenges such as external disturbances and coupling effects. In this article, a switching nonsingular terminal sliding mode control (NTSMC) method with a double-loop fuzzy neural network (DLFNN) is developed. This method enables the antagonistic PM-actuated wrist robots to achieve fast and precise tracking performance. Specifically, the lumped disturbances are estimated online using the DLFNN, which can adaptively adjust the weight of the inner and outer layers, achieving accurate approximation and robustness. Based on the estimated value of disturbances, a switching NTSMC is implemented to ensure that tracking errors converge to the origin within the fixed time. Switching functions guarantee fast convergence when the sliding surface errors are large. Meanwhile, switching functions ensure nonsingularity as the sliding surface errors converge to the origin. Furthermore, joint angles and angular velocities are limited within the specific ranges by designing exponential constraint terms as time-varying proportional-differential gains, rather than traditional barrier functions that may induce excessive control inputs. Both detailed stability analysis and experimental validation demonstrate the effectiveness and adaptability of the proposed method.**

***Index Terms*—Double-loop fuzzy neural networks (DLFNNs), fixed time, motion control, pneumatic muscles (PMs), switching control.**

Received 24 August 2025; revised 16 November 2025; accepted 12 December 2025. Date of publication 23 December 2025; date of current version 5 February 2026. This work was supported in part by the National Natural Science Foundation of China under Grant 62533014, Grant 62373198, and Grant 62303245, in part by the Natural Science Foundation of Tianjin under Grant 24JCZXJC00220, in part by the Beijing-Tianjin-Hebei Basic Research Cooperation Special Project under Grant F2024205028, in part by Guangdong Basic and Applied Basic Research Foundation under Grant 2025A1515011246, in part by Science and Technology Development Fund under Grant 001/2024/SKL, and in part by the State Key Laboratory of Internet of Things for Smart City (University of Macau) Open Research Project under Grant SKL-IoTSC(UM)/ORP07/2025. Recommended by Associate Editor H. Yan. *(Corresponding author: Ning Sun.)*

Yuexuan Xu is with the Institute of Robotics and Automatic Information Systems (IRAIS), College of Artificial Intelligence, and the Academy for Advanced Interdisciplinary Studies, Nankai University, Tianjin 300350, China, also with the Institute of Intelligence Technology and Robotic Systems, Shenzhen Research Institute of Nankai University, Shenzhen 518083, China, and also with the Department of Mechanical Engineering, The Hong Kong Polytechnic University, KLN Hong Kong (e-mail: xuyx@mail.nankai.edu.cn).

Shuzhen Diao, Tong Yang, and Xinlin Zhang are with the Institute of Robotics and Automatic Information Systems (IRAIS), College of Artificial Intelligence, and the Academy for Advanced Interdisciplinary Studies, Nankai University, Tianjin 300350, China, and also with the Institute of Intelligence Technology and Robotic Systems, Shenzhen Research Institute of Nankai University, Shenzhen 518083, China (e-mail: diaoshuzhen@mail.nankai.edu.cn; yangt@nankai.edu.cn; zhangxinlin@mail.nankai.edu.cn).

Ming Li is with the Shandong Inspur Database Technology Company, Ltd., Jinan 250000, China (e-mail: liming2017@inspur.com).

Yakun Gao is with the Inspur Intelligent Supply Chain Technology (Shandong) Company, Ltd., Jinan 250101, China (e-mail: gaoyakun@inspur.com).

David Navarro-Alarcon is with the Department of Mechanical Engineering, The Hong Kong Polytechnic University, KLN Hong Kong (e-mail: david.navarro-alarcon@polyu.edu.hk).

Ning Sun is with the Institute of Robotics and Automatic Information Systems (IRAIS), College of Artificial Intelligence, and the Academy for Advanced Interdisciplinary Studies, Nankai University, Tianjin 300350, China, also with the Institute of Intelligence Technology and Robotic Systems, Shenzhen Research Institute of Nankai University, Shenzhen 518083, China, and also with the Shenzhen Loop Area Institute, Shenzhen 518048, China (e-mail: sunn@nankai.edu.cn).

Digital Object Identifier 10.1109/TFUZZ.2025.3647090

## I. Introduction

STROKE has become a significant disease that poses a considerable threat to global health. Following a stroke, most survivors suffer from the inability to control their limbs, which significantly affects their quality of life. Upper limb dyskinesia is one of the most common disabilities among stroke patients [1]. Upper limb rehabilitation robots can not only relieve the pressure of therapists' manual operations, but also provide personalized, high-intensity, and multimode rehabilitation training [2], [3]. Due to the wrist joint's high flexibility and complex physiological structure, it is crucial in the design of upper limb exoskeleton robots [4]. Over the past decades, researchers have made great progress in developing flexible wrist robots for rehabilitation and assistive tasks.

Pneumatic muscles (PMs) are widely utilized in flexible wrist robots due to their excellent power-to-weight ratio [5], excellent flexibility [6], [7], compliance [8], and low costs [9]. Jeong et al. [10] designed a soft wrist exo-suit actuated by five McKibben-type PMs, achieving motion control in 2-degrees of freedom (DOF). Since a single PM can only exert unidirectional telescopic force, most PM-actuated wrist robots depend

on an antagonistic configuration. In [11], a 2-DOF fabric PM-actuated soft wrist exo-suit has been developed with two pairs of agonist-antagonistic PMs. However, the nonlinearity [12], hysteresis [13], creep [14], time-varying parameters [15], and unmodeled dynamics [16] caused by compressed gas, flexible materials, and structural characteristics seriously degrade the control performance and prevent the practical application of PMs. In addition, motion control of PMs necessitates crucial consideration of disturbance suppression, uncertainty compensation, and transient performance.

Based on the characteristics of PMs, many researchers are devoted to enhancing the motion control performance of PM-actuated robots. First, combined with feedforward compensation, traditional control methods can address motion control actuated by a PM or multiple PMs in simple scenarios. Lin et al. [17] and Xie et al. [18] proposed PI models and MS-GPI models to compensate for the PM hysteresis, respectively, integrating these approaches with PID control frameworks to achieve desired control performance. However, it remains challenging for traditional control methods to ensure control effectiveness under significant disturbances and parameter uncertainties in the system.

To enhance robustness against disturbances, researchers have developed several control methods, including sliding mode control (SMC) [19], optimal control [20], and active disturbance rejection control [21]. SMC has been extensively applied to PM-actuated robots because of its disturbance insensitivity and fast dynamic response. Nevertheless, the switching term of traditional SMC is discontinuous, which can cause chattering in practical applications. In [22], an SMC method has been proposed based on the tanh-type function to suppress the chattering problem of control inputs. By combining the SMC with advanced methods, such as adaptive control [23], [24]; neural networks [25], [26]; fuzzy control [27], [28]; and disturbance observers [29], modeling uncertainties and external disturbances can be effectively compensated. Qin et al. [30] designed an adaptive set-membership filter for estimating the nonlinear terms and external disturbances of PM-actuated robots. By combining this filter with SMC, precise tracking control is achieved. Additionally, utilizing the global approximation properties of neural networks, Cao et al. [31] developed an echo state network for online estimation of unmodeled dynamics in PM-actuated exoskeleton robots. Diao et al. [32] presented a novel fuzzy-based control method for 2-DOF PM-actuated robots, ensuring satisfactory tracking performance and velocity constraints. In [33], an adaptive fuzzy control method is proposed for PM angle tracking, where fuzzy logic systems approximate unknown nonparametric uncertainties and robust control methods compensate for the approximation errors. Chen et al. [34] proposed a deep fuzzy neural network integrating fuzzy logic and deep learning for pretrain-free real-time control of pneumatic systems.

Given the strong nonlinearities of PM-actuated robots, convergence time significantly impacts system performance. Slow convergence inevitably reduces working efficiency and degrades control accuracy. Consequently, finite-time [35], fixed-time (FT) [36], [37], and prescribed-time control methods [38] are developed to mitigate these problems. Zhang et al. [35] proposed an adaptive fuzzy switching control method that achieves finite-time convergence for PM-actuated parallel robots under uncertainties and disturbances. In [37], a nonlinear disturbance observer-based FT dynamic surface control method is proposed for trajectory tracking of PM-actuated robots, where variable gains are designed to achieve desired control performance.

Based on the preceding discussions, three key challenges in PM-actuated robots are summarized as follows.

1) *Tracking accuracy:* Numerous studies necessitate precise mathematical models. Under conditions of significant plant uncertainties or external disturbances, the system becomes susceptible to generating significant tracking errors, in severe cases, causing the tracking errors to fail to converge. More importantly, an essential issue for PM-actuated robots is guaranteeing asymptotic convergence without *prior* knowledge instead of uniformly ultimately bounded (UUB) results.
2) *Transient performance:* Many control methods can only achieve asymptotic stability of PM-actuated robots, which means that the convergence time is undefined. However, convergence time is usually strictly limited in practical scenarios, and then improving the convergence speed without being affected by the system's initial values is a critical research topic.
3) *Safe operation and hardware limits:* PM-actuated robots must operate within geometric and physical boundaries that impose necessary limitations on joint angles, positions, velocities, and other state variables. Specifically, for the antagonistic PM-actuated robots, the cooperative and competitive relationship between agonist-antagonist muscle pairs is more difficult to ensure satisfactory control performance, as excessive contraction of one muscle can generate harmful tension, leading to potential muscle damage or system instability.

To address the aforementioned problems, a double-loop fuzzy neural network (DLFNN)-based FT robust control method for antagonistic PM-actuated wrist robots is proposed. Then, the closed-loop system's stability is verified through rigorous mathematical analysis. Finally, the method's effectiveness is demonstrated through comprehensive experimental testing. The primary contributions of this article can be highlighted as follows.

1) Compared with some SMC methods [39], a switching nonsingular terminal sliding mode control (NTSMC) method is proposed to ensure that tracking errors converge to the origin without singularity. In addition, the proposed method guarantees tracking errors to approach the origin in a fixed time (rather than UUB convergence, e.g., in [40] and [41]), enhancing the response speed of the antagonistic PMs.
2) The DLFNN is introduced to realize online estimation of external disturbances, uncertainties, and coupling among antagonistic joints. The network contains two feedback loops: an external feedback loop in the output layer and an internal feedback loop in the fuzzification layer. Compared with the radial basis function neural network

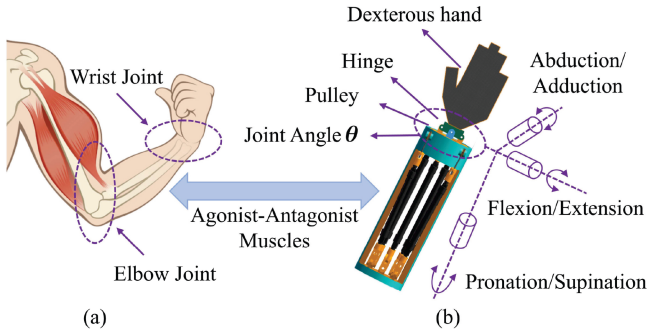


Fig. 1. (a) 3-DOF in the wrist and forearm. (b) Schematic of the antagonistic PM-actuated wrist robots.

(RBFNN) [42], the DLFNN has local and global memory capabilities, which effectively improve estimation accuracy, speed, and robustness.

3) The exponential constraint terms are designed to ensure that the angles and angular velocities of each antagonistic joint pair operate safely within predefined boundaries. Specifically, the exponential constraint terms are regarded as time-varying proportional-derivative gains, unlike traditional barrier functions (e.g., in [43] and [44]) that generate excessive control inputs and require more complex proof processes. More importantly, compared with [45] and [46], the exponential constraint terms can be applied with or without constraints.

The rest of this article is organized as follows. Section II introduces the antagonistic PM-actuated wrist robots and defines the control objectives. In Section III, a switching NTSMC method is developed by combining the DLFNN and motion constraints. Afterwards, the mathematical stability proof for the proposed control method is provided in Section IV. Apart from that, a series of experiments is executed in Section V to validate the effectiveness of the proposed method. Finally, Section VI concludes this article.

*Notation:* For $\boldsymbol{x}, \boldsymbol{y} \in \Re^n$, $\boldsymbol{x} \odot \boldsymbol{y}$ stands for the Hadamard product. Moreover, $\mathbf{sgn}(\boldsymbol{x})$ denotes the sign function, and the function $\mathbf{sig}(\boldsymbol{x})$ is defined as $\mathbf{sig}^p(\boldsymbol{x}) = \mathbf{sgn}(\boldsymbol{x}) \odot |\boldsymbol{x}|^p$. Define the vector multiplication operator $\circ$ such that for $\boldsymbol{a} \in \Re^m$ and $\boldsymbol{b} \in \Re^n$, the resulting vector $\boldsymbol{c} = \boldsymbol{a} \circ \boldsymbol{b} \in \Re^{mn}$ has elements $c_{(i-1)n+j} = a_i b_j$ for $i = 1, 2, \ldots, m$ and $j = 1, 2, \ldots, n$.

## II. Model Description and Problem Statement

### A. Dynamics of Antagonistic PM-Actuated Wrist Robots

Human wrist movements typically include 3-DOF: pronation and supination (PS), flexion and extension (FE), as well as abduction and adduction (AA), as depicted in Fig. 1(a). AA is also known as radial-ulnar deviation. Based on this, the antagonistic PM-actuated wrist robots are designed to simulate human wrist movements, as shown in Fig. 1(b). Six PMs are connected through hinges and a pulley to achieve 3-DOF movements. Specifically, two pairs of antagonistic PMs are connected through hinges to achieve FE and AA DOF movements, while one pair of antagonistic PMs is connected through a pulley to realize PS DOF movement. The drive units of antagonistic PMs

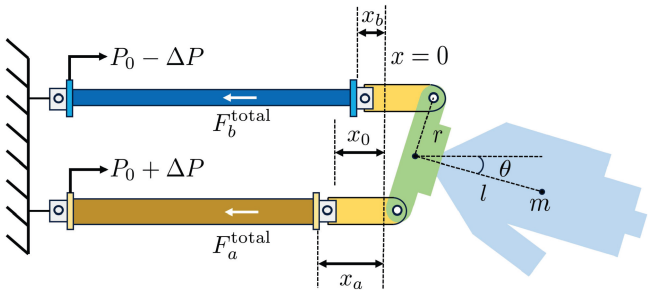


Fig. 2. Working principle of antagonistic PMs.

employ the following control method:[1]

$$\begin{cases} \boldsymbol{P}_a = \boldsymbol{P}_0 + \Delta \boldsymbol{P} \\ \boldsymbol{P}_b = \boldsymbol{P}_0 - \Delta \boldsymbol{P} \end{cases} \tag{1}$$

where $\boldsymbol{P}_a \in \Re^3$ and $\boldsymbol{P}_b \in \Re^3$ represent the internal pressure of the agonist and antagonistic PMs, respectively, $\boldsymbol{P}_0 \in \Re^3$ denotes the nominal value of air pressure, and $\Delta \boldsymbol{P} \in \Re^3$ is the pressure change as the control input for the driving unit. Once $\boldsymbol{P}_0$ is set, the three pairs of proportional valves can be uniformly controlled, and the six PMs have the initial displacement $\boldsymbol{x}_0$. When agonist PMs inflate, antagonistic PMs deflate, thereby driving the corresponding joint rotation motion, as shown in Fig. 2. Furthermore, the dynamic behavior of a single PM can be characterized by a damping element, a spring element, and a contraction element, which can be described as [47]

$$M_a \ddot{x} + B(P)\dot{x} + K(P)x = F(P) - M_a g \tag{2}$$

where $x$ denotes the PM displacement, $P$ represents the internal pressure of the PM, $g$ is the gravitational acceleration, and $M_a$, $B(P)$, $K(P)$, $F(P)$ stand for the payload mass, the damping force, the spring force, and the contractile force, respectively, which can be obtained as follows:

$$\begin{cases} B(P) = B_{0,j} + B_{1,j} P \\ K(P) = K_0 + K_1 P \\ F(P) = F_0 + F_1 P \end{cases} \tag{3}$$

where $K_0$, $K_1$ are the spring coefficient, $B_{0,j}$, $B_{1,j}$ are the damping coefficient, $F_0$, $F_1$ are the contractile force coefficient, and $j = 1, 2$ denotes the contraction and deflation state of the PM, respectively. Hence, the total force $F^{\text{total}}$ exerted by the PM is expressed as

$$F^{\text{total}} = F(P) - B(P)\dot{x} - K(P)x. \tag{4}$$

According to Fig. 2, the initial displacement of the agonist and antagonistic PMs in a pair of antagonistic PMs is represented as $x_0$, which can determine the initial angle $\theta(0) = 0$ of the hinge and pulley. The torque $T$ produced by the agonist and antagonistic PMs is derived as

$$\begin{cases} T = (F_a^{\text{total}} - F_b^{\text{total}}) r \cos\theta, \text{ FE and AA DOF} \\ T = (F_a^{\text{total}} - F_b^{\text{total}}) r, \text{ PS DOF} \end{cases} \tag{5}$$

[1]For convenience of the subsequent expressions, any information related to the state or time is omitted unless it is necessary to present.

where $r$ denotes the pulley radius and half of the hinge length, $\theta$ stands for the joint angles of pulley and hinge, and $F_a^{\text{total}}$, $F_b^{\text{total}}$ are the force exerted by the agonist and antagonistic PMs, respectively

$$\begin{cases} F_a^{\text{total}} = F_a(P_a) - B_a(P_a)\dot{x}_a - K_a(P_a)x_a \\ F_b^{\text{total}} = F_b(P_b) - B_b(P_b)\dot{x}_b - K_b(P_b)x_b \end{cases} \tag{6}$$

where $x_a$ and $x_b$ are determined by $x_0$

$$\begin{cases} x_a = x_0 + r\sin\theta, \ \text{FE and AA DOF} \\ x_b = x_0 - r\sin\theta, \ \text{FE and AA DOF} \\ x_a = x_0 + r\theta, \ \text{PS DOF} \\ x_b = x_0 - r\theta, \ \text{PS DOF}. \end{cases} \tag{7}$$

Combined with (4), (5), (6), and (7), we can obtain that[2]

$$\begin{aligned} T = J\ddot{\theta} &= \left(F_a^{\text{total}} - F_b^{\text{total}}\right) r - mgl\sin\theta + d_0 \\ &= \left(F_{0a} + F_{1a}P_a\right) r - \left(B_{0a} + B_{1a}P_a\right)\dot{x}_a r \\ &\quad - \left(K_{0a} + K_{1a}P_a\right) x_a r - \left(F_{0b} + F_{1b}P_b\right) r \\ &\quad + \left(B_{0b} + B_{1b}P_b\right)\dot{x}_b r + \left(K_{0b} + K_{1b}P_b\right) x_b r \\ &\quad - mgl\sin\theta + d_0 = \rho_0 + \rho_1\Delta P + d_0 \end{aligned} \tag{8}$$

where $J$ represents the moment of inertia, $m$ denotes the equivalent payload mass, $d_0$ stands for the lumped disturbances, including external disturbances, friction, hysteresis, creep, and other inherent characteristics in PMs, and $l$ is the equivalent length from the centroid of the pulley or hinge to the centroid of the dexterous hand. The mathematical expressions for $\rho_0$ and $\rho_1$ are presented as follows:

$$\begin{cases} \rho_0 = \lambda_1 - \lambda_2\dot{\theta} - \lambda_3\theta - \lambda_4 - mgl\sin\theta \\ \rho_1 = \lambda_5 + \lambda_6\dot{\theta} + \lambda_7\theta - \lambda_8 \\ \lambda_1 = \left(F_{0a} + F_{1a}P_0 - F_{0b} - F_{1b}P_0\right) r \\ \lambda_2 = \left(B_{0a} + B_{1a}P_0 + B_{0b} + B_{1b}P_0\right) r^2 \\ \lambda_3 = \left(K_{0a} + K_{1a}P_0 + K_{0b} + K_{1b}P_0\right) r^2 \\ \lambda_4 = \left(K_{0a} + K_{1a}P_0 - K_{0b} - K_{1b}P_0\right) r x_0 \\ \lambda_5 = \left(F_{1a} + F_{1b}\right) r \\ \lambda_6 = \left(B_{1b} - B_{1a}\right) r \\ \lambda_7 = \left(K_{1b} - K_{1a}\right) r^2 \\ \lambda_8 = \left(K_{1a} + K_{1b}\right) r x_0. \end{cases} \tag{9}$$

Consequently, the general dynamics of the antagonistic PM-actuated wrist robots under uncertainties and disturbances are represented as follows:

$$\boldsymbol{M}\odot\ddot{\boldsymbol{\theta}} + \boldsymbol{f}(\boldsymbol{\theta},\dot{\boldsymbol{\theta}}) + \boldsymbol{d}_L = \boldsymbol{u} \tag{10}$$

where $\boldsymbol{\theta} = [\theta_1,\theta_2,\theta_3]^T$, $\dot{\boldsymbol{\theta}} = [\dot{\theta}_1,\dot{\theta}_2,\dot{\theta}_3]^T$, $\boldsymbol{u} = [u_1,u_2,u_3]^T$ is the control inputs and $\boldsymbol{u} = \Delta\boldsymbol{P}$, $\boldsymbol{M} = [M_1,M_2,M_3]^T$ and $M_i = J/\rho_1$, $\boldsymbol{f}(\boldsymbol{\theta},\dot{\boldsymbol{\theta}}) = [f_1,f_2,f_3]^T$ and $f_i = -\rho_0/\rho_1$, $\boldsymbol{d}_L = [d_{L1},d_{L2},d_{L3}]^T$ and $d_{Li} = -d_0/\rho_1$ with $i = 1,2,3$. In practical applications, $\boldsymbol{d}_L$ is bounded and satisfies $\|\boldsymbol{d}_L\| < \bar{d}$. Afterwards, (10) can be rearranged as follows:

$$\begin{aligned} \ddot{\boldsymbol{\theta}} &= \boldsymbol{M}^{-1}\odot\boldsymbol{u} - \boldsymbol{M}^{-1}\odot\left[\boldsymbol{f}(\boldsymbol{\theta},\dot{\boldsymbol{\theta}}) + \boldsymbol{d}_L\right] \\ &= \boldsymbol{M}_*\odot\boldsymbol{u} + \Delta\boldsymbol{M}\odot\boldsymbol{u} - \boldsymbol{M}^{-1}\odot\left[\boldsymbol{f}(\boldsymbol{\theta},\dot{\boldsymbol{\theta}}) + \boldsymbol{d}_L\right] \\ &= \boldsymbol{M}_*\odot\boldsymbol{u} + \boldsymbol{D}(\boldsymbol{\theta},\dot{\boldsymbol{\theta}},\boldsymbol{u}) \end{aligned} \tag{11}$$

where $\boldsymbol{M}^{-1} = \boldsymbol{M}_* + \Delta\boldsymbol{M}$, $\boldsymbol{M}_* \in \Re^3$ represents the nominal vector, $\Delta\boldsymbol{M} \in \Re^3$ stands for unmodeled dynamics of $\boldsymbol{M}^{-1}$, and $\boldsymbol{D}(\boldsymbol{\theta},\dot{\boldsymbol{\theta}},\boldsymbol{u}) = [D_1,D_2,D_3]^T$ contains unmodeled dynamics, uncertainties as well as lumped disturbances.

### B. Control Objectives

For the FT control of antagonist PM-actuated wrist robots in (10) with plant uncertainties and lumped disturbances, the main control objectives are summarized as follows.

1) Ensure the joint angle and angular velocity signals converge to the desired trajectories in the fixed time, i.e.,

$$\lim_{t\to T}[\boldsymbol{\theta}(t) - \boldsymbol{\theta}_d(t)] = \boldsymbol{0}, \ \lim_{t\to T}[\dot{\boldsymbol{\theta}}(t) - \dot{\boldsymbol{\theta}}_d(t)] = \boldsymbol{0} \tag{12}$$

where $\boldsymbol{\theta}_d(t) = [\theta_{d1}(t), \theta_{d2}(t), \theta_{d3}(t)]^T$ and $\dot{\boldsymbol{\theta}}_d(t) = [\dot{\theta}_{d1}(t), \dot{\theta}_{d2}(t), \dot{\theta}_{d3}(t)]^T$ denote the desired joint angle and angular velocity signals, respectively.

2) The joint angles $\boldsymbol{\theta}(t)$ and angular velocities $\dot{\boldsymbol{\theta}}(t)$ are constrained to operate within the predefined ranges

$$\boldsymbol{\theta} \in (-\bar{\boldsymbol{\theta}},\bar{\boldsymbol{\theta}}), \ \dot{\boldsymbol{\theta}} \in (-\bar{\boldsymbol{\theta}}_v,\bar{\boldsymbol{\theta}}_v) \tag{13}$$

where $\bar{\boldsymbol{\theta}} = [\bar{\theta}_1,\bar{\theta}_2,\bar{\theta}_3]^T$ and $\bar{\boldsymbol{\theta}}_v = [\bar{\theta}_{v1},\bar{\theta}_{v2},\bar{\theta}_{v3}]^T$ represent the predefined constraints for the joint angles and angular velocities, respectively.

*Lemma 1 (See [49]):* Consider the system $\dot{\boldsymbol{x}} = \boldsymbol{f}(\boldsymbol{x},t)$ where $\boldsymbol{x} \in \Re^n$ and $\boldsymbol{f} : \Re^n \times \Re_+ \to \Re^n$ is a nonlinear function. If there exists a continuous positive definite function $V(\boldsymbol{x}) : \Re^n \to \Re$ and positive constants $\alpha,\beta,m,n,p,q$ such that $\dot{V} \le -\alpha V^{m/n} - \beta V^{p/q}$ with $m > n$ and $p < q$, then the origin of the closed-loop system is FT stable. The settling time $T_a$ satisfies

$$T_a = \frac{1}{\alpha}\frac{n}{m-n} + \frac{1}{\beta}\frac{q}{q-p}.$$

## III. Controller Design

This section details a DLFNN to estimate the uncertainties and lumped disturbances for the antagonistic PM-actuated wrist robots (10). Subsequently, a switching NTSMC is constructed to achieve FT convergence of the tracking errors to the origin. Meanwhile, two constraint terms are designed to limit the joint angles and angular velocities within the safety ranges. The corresponding diagram of the proposed method is depicted in Fig. 3.

[2]For convenience of the subsequent expressions, (8) and (9) only present the modeling for the PS DOF. The modeling principles for FE and AA DOF are identical and thus omitted here.

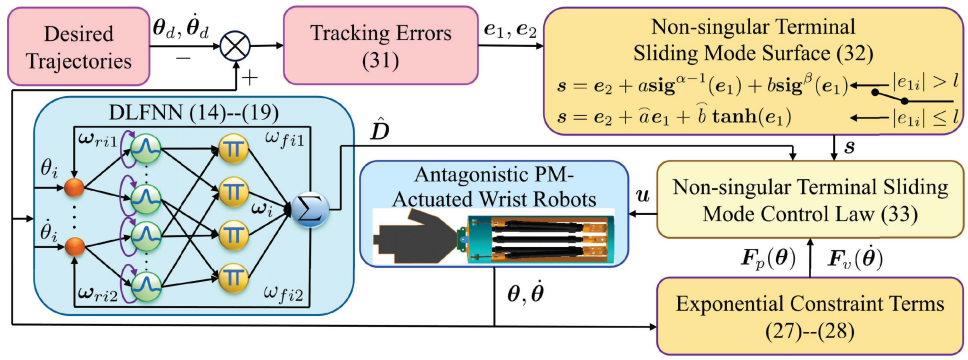


Fig. 3. Control flow diagram of the proposed method.

### A. DLFNN Design

The DLFNN consists of four layers: input layer, fuzzification layer, rule layer, and output layer, as shown in Fig. 3. Each layer's signal flow and functions are detailed as follows.

*Layer 1: Input layer:* The input layer is to receive the input signals $X_{im}^{(1)}(T) = [X_{i1}(T), X_{i2}(T)]^T$ and the feedback signals from the output layer $Y_i^{(4)}(T-1)$, where $i = 1, 2, 3$ is three pairs of antagonistic joints, $m = 1, 2$ stands for joint angle and angular velocity signals, and $T$ denotes the $T$th sampling period. The outer loop feedback weights of DLFNN $\omega_{fim} = [\omega_{fi1}, \omega_{fi2}]^T$ are utilized to connect the input and output layers. The output signals of the input layer $Y_{im}^{(1)}(T) = [Y_{i1}^{(1)}(T), Y_{i2}^{(1)}(T)]^T$ can be represented as

$$Y_{im}^{(1)}(T) = X_{im}^{(1)}(T)\omega_{fim}Y_i^{(4)}(T-1). \tag{14}$$

*Layer 2: Fuzzification layer:* The processed signals are derived by calculating the weighted sum of the fuzzification layer's input and output signals. The inner loop feedback weights of DLFNN are used to connect the input and output signals of the fuzzification layer. Gaussian fuzzification functions are applied to the processed signals to obtain the corresponding affiliation [48], which is formulated as

$$Y_{i1k}^{(2)}(T) = \exp\left(-\frac{\left\|Y_{i1}^{(1)}(T) + \omega_{ri1k}Y_{i1k}^{(2)}(T-1) - c_{i1k}\right\|^2}{b_{i1k}^2}\right) \tag{15}$$

$$Y_{i2j}^{(2)}(T) = \exp\left(-\frac{\left\|Y_{i2}^{(1)}(T) + \omega_{ri2j}Y_{i2j}^{(2)}(T-1) - c_{i2j}\right\|^2}{b_{i2j}^2}\right) \tag{16}$$

where $k = 1, 2, \ldots, 11$, $j = 1, 2, \ldots, 11$, $\omega_{ri1k}$, and $\omega_{ri2j}$ are the inner loop feedback weights of DLFNN, $c_{i1k}$ and $c_{i2j}$ are the center values, $b_{i1k}$ and $b_{i2j}$ are the base width.

*Layer 3: Rule layer:* The rule layer applies multiplication operations to the fuzzification layer outputs. Therefore, the rule layer outputs are computed as

$$\phi_{in}^{(3)} = Y_{i1k}^{(2)} \circ Y_{i2j}^{(2)} \tag{17}$$

where $n = 11 \times (i-1) + j$ and $\boldsymbol{\phi}_i^{(3)} \in \Re^{121}$.

*Layer 4: Output layer:* Layer 4 contains a single node that computes the weighted sum of all Layer 3 nodes. The output values are calculated as

$$Y_i^{(4)} = \sum_{n=1}^{121} \omega_{in}\phi_{in}^{(3)} \tag{18}$$

where $\omega_{in}$ denotes the network weights. The DLFNN is utilized to approximate $\boldsymbol{D}(\boldsymbol{\theta}, \dot{\boldsymbol{\theta}}, \boldsymbol{u})$, and the approximated vector $\hat{\boldsymbol{D}} = [\hat{D}_1, \hat{D}_2, \hat{D}_3]^T$ is expressed as follows:

$$\hat{D}_i = \hat{\boldsymbol{\omega}}_i^T\hat{\boldsymbol{\phi}}_i(\boldsymbol{X}_i, \hat{\boldsymbol{\omega}}_{fi}, \hat{\boldsymbol{\omega}}_{ri1}, \hat{\boldsymbol{\omega}}_{ri2}) \tag{19}$$

where $\boldsymbol{X}_i = [\theta_i, \dot{\theta}_i]^T$, the estimated values $\hat{\boldsymbol{\omega}}_i$, $\hat{\boldsymbol{\omega}}_{fi}$, $\hat{\boldsymbol{\omega}}_{ri1}$, and $\hat{\boldsymbol{\omega}}_{ri2}$ can be updated online via the adaptive law. There are optimal weights $\boldsymbol{\omega}_i^*$, optimal inner loop feedback weights $\boldsymbol{\omega}_{ri1}^*$, $\boldsymbol{\omega}_{ri2}^*$, and optimal outer loop feedback weights $\boldsymbol{\omega}_{fi}^*$ to accurately estimate $\boldsymbol{D}(\boldsymbol{\theta}, \dot{\boldsymbol{\theta}}, \boldsymbol{u})$, i.e., $D_i(\theta_i, \dot{\theta}_i, u_i) = \boldsymbol{\omega}_i^{*T}\boldsymbol{\phi}_i^*(\boldsymbol{X}_i, \boldsymbol{\omega}_{fi}^*, \boldsymbol{\omega}_{ri1}^*, \boldsymbol{\omega}_{ri2}^*) + \sigma_i$. $\sigma_i$ denotes reconstruction errors with upper bounds, i.e., $||\boldsymbol{\sigma}|| \le \bar{\sigma}$ with $\boldsymbol{\sigma} = [\sigma_1, \sigma_2, \sigma_3]^T$. The approximation errors for DLFNN parameters can be denoted as follows:

$$\begin{cases} \tilde{\boldsymbol{\omega}}_i = \boldsymbol{\omega}_i^* - \hat{\boldsymbol{\omega}}_i \\ \tilde{\boldsymbol{\omega}}_{fi} = \boldsymbol{\omega}_{fi}^* - \hat{\boldsymbol{\omega}}_{fi} \\ \tilde{\boldsymbol{\omega}}_{ri1} = \boldsymbol{\omega}_{ri1}^* - \hat{\boldsymbol{\omega}}_{ri1} \\ \tilde{\boldsymbol{\omega}}_{ri2} = \boldsymbol{\omega}_{ri2}^* - \hat{\boldsymbol{\omega}}_{ri2} \end{cases}. \tag{20}$$

Afterwards, the approximation errors $\tilde{\boldsymbol{D}} = [\tilde{D}_1, \tilde{D}_2, \tilde{D}_3]^T$ of the DLFNN can be derived as

$$\begin{aligned} \tilde{D}_i &= D_i(\theta_i, \dot{\theta}_i, u_i) - \hat{D}_i \\ &= \boldsymbol{\omega}_i^{*T}\boldsymbol{\phi}_i^* + \sigma_i - \hat{\boldsymbol{\omega}}_i^T\hat{\boldsymbol{\phi}}_i \\ &= \left(\tilde{\boldsymbol{\omega}}_i^T + \hat{\boldsymbol{\omega}}_i^T\right)\left(\tilde{\boldsymbol{\phi}}_i + \hat{\boldsymbol{\phi}}_i\right) - \hat{\boldsymbol{\omega}}_i^T\hat{\boldsymbol{\phi}}_i + \sigma_i \\ &= \hat{\boldsymbol{\omega}}_i^T\tilde{\boldsymbol{\phi}}_i + \tilde{\boldsymbol{\omega}}_i^T\hat{\boldsymbol{\phi}}_i + \delta_i \end{aligned} \tag{21}$$

where the total integrated approximation errors are $\delta_i = \sigma_i + \tilde{\boldsymbol{\omega}}_i^T\tilde{\boldsymbol{\phi}}_i$ and $\delta_i$ exists upper bounds [48]. Consequently, $\tilde{D}_i$ exists upper bounds, i.e., $|\tilde{D}_i| \le \Delta_0$.

Then, motivated by the first-order Taylor's series method, $\tilde{\phi}_i$ is derived as follows:

$$\begin{aligned}\tilde{\phi}_i &= \left.\frac{\partial\hat{\phi}_i}{\partial\boldsymbol{\omega}_{fi}}\right|_{\boldsymbol{\omega}_{fi}=\hat{\boldsymbol{\omega}}_{fi}}\tilde{\boldsymbol{\omega}}_{fi} + \left.\frac{\partial\hat{\phi}_i}{\partial\boldsymbol{\omega}_{ri1}}\right|_{\boldsymbol{\omega}_{ri1}=\hat{\boldsymbol{\omega}}_{ri1}}\tilde{\boldsymbol{\omega}}_{ri1} \\ &\quad + \left.\frac{\partial\hat{\phi}_i}{\partial\boldsymbol{\omega}_{ri2}}\right|_{\boldsymbol{\omega}_{ri2}=\hat{\boldsymbol{\omega}}_{ri2}}\tilde{\boldsymbol{\omega}}_{ri2} + \boldsymbol{o}_i \\ &= \partial\hat{\boldsymbol{\phi}}_{\boldsymbol{\omega}_{fi}}\tilde{\boldsymbol{\omega}}_{fi} + \partial\hat{\boldsymbol{\phi}}_{\boldsymbol{\omega}_{ri1}}\tilde{\boldsymbol{\omega}}_{ri1} + \partial\hat{\boldsymbol{\phi}}_{\boldsymbol{\omega}_{ri2}}\tilde{\boldsymbol{\omega}}_{ri2} + \boldsymbol{o}_i \end{aligned} \tag{22}$$

where $\boldsymbol{o}_i \in \Re^{121}$ is the high-order residual term and $\partial\hat{\boldsymbol{\phi}}_{\boldsymbol{\omega}_{fi}}$, $\partial\hat{\boldsymbol{\phi}}_{\boldsymbol{\omega}_{ri1}}$, $\partial\hat{\boldsymbol{\phi}}_{\boldsymbol{\omega}_{ri2}}$ can be represented as

$$\partial\hat{\boldsymbol{\phi}}_{\boldsymbol{\omega}_{fi}} = \left.\begin{bmatrix} \frac{\partial\hat{\phi}_{i1}}{\partial\omega_{fi1}} & \frac{\partial\hat{\phi}_{i2}}{\partial\omega_{fi1}} & \cdots & \frac{\partial\hat{\phi}_{i121}}{\partial\omega_{fi1}} \\ \frac{\partial\hat{\phi}_{i1}}{\partial\omega_{fi2}} & \frac{\partial\hat{\phi}_{i2}}{\partial\omega_{fi2}} & \cdots & \frac{\partial\hat{\phi}_{i121}}{\partial\omega_{fi2}} \end{bmatrix}^T\right|_{\boldsymbol{\omega}_{fi}=\hat{\boldsymbol{\omega}}_{fi}} \tag{23}$$

$$\partial\hat{\boldsymbol{\phi}}_{\boldsymbol{\omega}_{ri1}} = \left.\begin{bmatrix} \frac{\partial\hat{\phi}_{i1}}{\partial\omega_{ri1,1}} & \cdots & \frac{\partial\hat{\phi}_{i1}}{\partial\omega_{ri1,k}} & \cdots & \frac{\partial\hat{\phi}_{i1}}{\partial\omega_{ri1,11}} \\ \vdots & \ddots & \vdots & & \vdots \\ \frac{\partial\hat{\phi}_{in}}{\partial\omega_{ri1,1}} & \cdots & \frac{\partial\hat{\phi}_{in}}{\partial\omega_{ri1,k}} & \cdots & \frac{\partial\hat{\phi}_{in}}{\partial\omega_{ri1,11}} \\ \vdots & & \vdots & \ddots & \vdots \\ \frac{\partial\hat{\phi}_{i121}}{\partial\omega_{ri1,1}} & \cdots & \frac{\partial\hat{\phi}_{i121}}{\partial\omega_{ri1,k}} & \cdots & \frac{\partial\hat{\phi}_{i121}}{\partial\omega_{ri1,11}} \end{bmatrix}\right|_{\boldsymbol{\omega}_{ri1}=\hat{\boldsymbol{\omega}}_{ri1}} \tag{24}$$

$$\partial\hat{\boldsymbol{\phi}}_{\boldsymbol{\omega}_{ri2}} = \left.\begin{bmatrix} \frac{\partial\hat{\phi}_{i1}}{\partial\omega_{ri2,1}} & \cdots & \frac{\partial\hat{\phi}_{i1}}{\partial\omega_{ri2,j}} & \cdots & \frac{\partial\hat{\phi}_{i1}}{\partial\omega_{ri2,11}} \\ \vdots & \ddots & \vdots & & \vdots \\ \frac{\partial\hat{\phi}_{in}}{\partial\omega_{ri2,1}} & \cdots & \frac{\partial\hat{\phi}_{in}}{\partial\omega_{ri2,j}} & \cdots & \frac{\partial\hat{\phi}_{in}}{\partial\omega_{ri2,11}} \\ \vdots & & \vdots & \ddots & \vdots \\ \frac{\partial\hat{\phi}_{i121}}{\partial\omega_{ri2,1}} & \cdots & \frac{\partial\hat{\phi}_{i121}}{\partial\omega_{ri2,j}} & \cdots & \frac{\partial\hat{\phi}_{i121}}{\partial\omega_{ri2,11}} \end{bmatrix}\right|_{\boldsymbol{\omega}_{ri2}=\hat{\boldsymbol{\omega}}_{ri2}} \tag{25}$$

where $\partial\hat{\boldsymbol{\phi}}_{\boldsymbol{\omega}_{fi}} \in \Re^{121\times 2}$, $\partial\hat{\boldsymbol{\phi}}_{\boldsymbol{\omega}_{ri1}} \in \Re^{121\times 11}$, and $\partial\hat{\boldsymbol{\phi}}_{\boldsymbol{\omega}_{ri2}} \in \Re^{121\times 11}$. Taking (22)–(25) into (21), we finally obtain

$$\begin{aligned}\tilde{D}_i &= \tilde{\boldsymbol{\omega}}_i^T\hat{\boldsymbol{\phi}}_i + \hat{\boldsymbol{\omega}}_i^T(\partial\hat{\boldsymbol{\phi}}_{\boldsymbol{\omega}_{fi}}\tilde{\boldsymbol{\omega}}_{fi} + \partial\hat{\boldsymbol{\phi}}_{\boldsymbol{\omega}_{ri1}}\tilde{\boldsymbol{\omega}}_{ri1} + \partial\hat{\boldsymbol{\phi}}_{\boldsymbol{\omega}_{ri2}}\tilde{\boldsymbol{\omega}}_{ri2}) \\ &\quad + \hat{\boldsymbol{\omega}}_i^T\boldsymbol{o}_i + \delta_i. \end{aligned} \tag{26}$$

### B. Exponential Constraint Terms

To ensure the safe operation of the antagonistic PM-actuated wrist robots, two exponential constraint terms $\boldsymbol{F}_p(\boldsymbol{\theta}) = [F_{p1}, F_{p2}, F_{p3}]^T$ and $\boldsymbol{F}_v(\dot{\boldsymbol{\theta}}) = [F_{v1}, F_{v2}, F_{v3}]^T$ are constructed to limit the angle and angular velocity of each antagonistic joint, as follows:

$$F_{pi}(\theta_i) = k_p\bar{\theta}_i^2\left[\exp\left(\frac{\theta_i^2}{\bar{\theta}_i^2-\theta_i^2}\right)-1\right] \tag{27}$$

$$F_{vi}(\dot{\theta}_i) = k_v\bar{\theta}_{vi}^2\left[\exp\left(\frac{\dot{\theta}_i^2}{\bar{\theta}_{vi}^2-\dot{\theta}_i^2}\right)-1\right] \tag{28}$$

where $k_p$ and $k_v$ are positive parameters and $i = 1, 2, 3$. The initial states are selected within the predefined constraints, that is, $\theta_i(0) \in (-\bar{\theta}_i, \bar{\theta}_i)$ and $\dot{\theta}_i(0) \in (-\bar{\theta}_{vi}, \bar{\theta}_{vi})$. Notably, the exponential constraint terms are time-varying positive definite functions. If there are no constraint requirements on angles and angular velocities, assuming $\bar{\theta}_i$ and $\bar{\theta}_{vi}$ approach infinity, we can obtain the following conclusions by L'Hopital's rule:

$$\lim_{\bar{\theta}_i\to\infty} k_p\bar{\theta}_i^2\left[\exp\left(\frac{\theta_i^2}{\bar{\theta}_i^2-\theta_i^2}\right)-1\right] = k_p\theta_i^2 \tag{29}$$

$$\lim_{\bar{\theta}_{vi}\to\infty} k_v\bar{\theta}_{vi}^2\left[\exp\left(\frac{\dot{\theta}_i^2}{\bar{\theta}_{vi}^2-\dot{\theta}_i^2}\right)-1\right] = k_v\dot{\theta}_i^2. \tag{30}$$

If there are no constraints, the exponential constraint terms are reduced to proportional-derivative gains. Thus, it can work in both constrained and unconstrained cases.

### C. Controller Development

In this section, a switching NTSMC is proposed based on the estimated values of DLFNN to fulfill the control objectives in (12) and (13). First, the tracking errors of joint angles $\boldsymbol{\theta}$ and angular velocities $\dot{\boldsymbol{\theta}}$ are defined as

$$\begin{cases}\boldsymbol{e}_1 = \boldsymbol{\theta} - \boldsymbol{\theta}_d = [e_{11}, e_{12}, e_{13}]^T \\ \boldsymbol{e}_2 = \dot{\boldsymbol{\theta}} - \dot{\boldsymbol{\theta}}_d = [e_{21}, e_{22}, e_{23}]^T.\end{cases} \tag{31}$$

Then, the nonsingular terminal sliding surface function $\boldsymbol{s} = [s_1, s_2, s_3]^T$ is designed as follows:

$$\boldsymbol{s} = \begin{cases}\boldsymbol{e}_2 + a\mathbf{sig}^{\alpha-1}(\boldsymbol{e}_1) + b\mathbf{sig}^{\beta}(\boldsymbol{e}_1), |e_{1i}| > l \\ \boldsymbol{e}_2 + \widehat{a}\,\boldsymbol{e}_1 + \widehat{b}\,\mathbf{tanh}(\boldsymbol{e}_1), |e_{1i}| \le l\end{cases} \tag{32}$$

where $a$, $b$, $\widehat{a}$, $\widehat{b}$, $\alpha$, $\beta$, $l$ are positive constants, $1 < \alpha < 2$, $\beta > 1$, $i = 1, 2, 3$. Then, an NTSMC law is formulated as

$$\boldsymbol{u} = \begin{cases}\boldsymbol{M}_*^{-1}\odot[-\hat{\boldsymbol{D}} + \ddot{\boldsymbol{\theta}}_d - a(\alpha-1)\mathbf{sig}^{\alpha-2}(\boldsymbol{e}_1)\odot\boldsymbol{e}_2 \\ -b\beta\mathbf{sig}^{\beta-1}(\boldsymbol{e}_1)\odot\boldsymbol{e}_2 - k_1\mathbf{sig}^{\alpha-1}(\boldsymbol{s}) - k_2\mathbf{sig}^{\beta}(\boldsymbol{s}) \\ -k_3\mathbf{tanh}(\boldsymbol{s}) - \boldsymbol{s}\odot(\boldsymbol{F}_p + \boldsymbol{F}_v)], |e_{1i}| \ge l \\ \boldsymbol{M}_*^{-1}\odot[-\hat{\boldsymbol{D}} + \ddot{\boldsymbol{\theta}}_d - \widehat{a}\,\boldsymbol{e}_2 - k_1\mathbf{sig}^{\alpha-1}(\boldsymbol{s}) - k_2\mathbf{sig}^{\beta}(\boldsymbol{s}) \\ -\widehat{b}\,(\mathbf{1} - \mathbf{tanh}(\boldsymbol{e}_1)\odot\mathbf{tanh}(\boldsymbol{e}_1))\odot\boldsymbol{e}_2 - k_3\mathbf{tanh}(\boldsymbol{s}) \\ -\boldsymbol{s}\odot(\boldsymbol{F}_p + \boldsymbol{F}_v)], |e_{1i}| < l\end{cases} \tag{33}$$

where $k_1 = \mathrm{diag}\{k_{11}, k_{12}, k_{13}\}$, $k_2 = \mathrm{diag}\{k_{21}, k_{22}, k_{23}\}$, $k_3 = \mathrm{diag}\{k_{31}, k_{32}, k_{33}\}$ are positive-definite diagonal matrices that serve as control gains for the controller.

## IV. Stability Analysis

This section will provide a strict Lyapunov-based stability analysis for the proposed controller.

*Theorem 1:* The NTSMC in (32) is continuous and differentiable at $|e_{1i}| = l$ with $i = 1, 2, 3$.

*Proof:* We will first prove the continuity of sliding surface functions. According to (32), we can obtain that

$$\begin{cases}\lim\limits_{|e_{1i}|\to l^+} s_i = e_{2i} + al^{\alpha-1} + bl^{\beta} \\ \lim\limits_{|e_{1i}|\to l^-} s_i = e_{2i} + \widehat{a}\,l + \widehat{b}\,\tanh(l).\end{cases} \tag{34}$$

The sliding surface function $s_i$ is continuous at $|e_{1i}| = l$ if and only if $\lim_{|e_{1i}|\to l^+} s_i = \lim_{|e_{1i}|\to l^-} s_i$. Hence, it is derived that

$$al^{\alpha-1} + bl^{\beta} = \widehat{a}\, l + \widehat{b}\, \tanh(l). \tag{35}$$

We will further demonstrate the differentiability of the sliding surface function. According to the definition of differentiability, we can obtain that

$$\begin{aligned}
&\lim_{\Delta x\to 0^+} \frac{s_i\,(l+\Delta x) - s_i(l)}{\Delta x} \\
&= \lim_{\Delta x\to 0^+} \frac{a(l+\Delta x)^{\alpha-1} + b(l+\Delta x)^{\beta} - \widehat{a}\, l - \widehat{b}\, \tanh(l)}{\Delta x} \\
&= \lim_{\Delta x\to 0^+} \frac{a(l+\Delta x)^{\alpha-1} - al^{\alpha-1} + b(l+\Delta x)^{\beta} - bl^{\beta}}{\Delta x} \\
&= a\,(\alpha-1)\, l^{\alpha-2} + b\beta l^{\beta-1}
\end{aligned} \tag{36}$$

$$\begin{aligned}
&\lim_{\Delta x\to 0^-} \frac{s_i\,(l+\Delta x) - s_i(l)}{\Delta x} \\
&= \lim_{\Delta x\to 0^-} \frac{\widehat{a}\,(l+\Delta x) + \widehat{b}\,\tanh\,(l+\Delta x) - \widehat{a}\, l - \widehat{b}\,\tanh(l)}{\Delta x} \\
&= \widehat{a} + \widehat{b}\,\left(1 - \tanh^2(l)\right).
\end{aligned} \tag{37}$$

The sliding surface functions are differentiable at $|e_{1i}| = l$ if and only if $\lim_{\Delta x\to 0^+} \frac{s_i(l+\Delta x) - s_i(l)}{\Delta x} = \lim_{\Delta x\to 0^-} \frac{s_i(l+\Delta x) - s_i(l)}{\Delta x}$. Therefore, we can derive that

$$a\,(\alpha-1)\, l^{\alpha-2} + b\beta l^{\beta-1} = \widehat{a} + \widehat{b}\,\left(1 - \tanh^2(l)\right). \tag{38}$$

In summary, when (35) and (38) hold simultaneously, the sliding surface function in (32) is continuous and differentiable at $|e_{1i}| = l$.

*Theorem 2:* For the antagonistic PM-actuated wrist robots in (10) with unmodeled dynamics, uncertainties, and lumped disturbances, by employing DLFNN and the proposed control method in (33), the tracking errors $\boldsymbol{e}_1$ and $\boldsymbol{e}_2$ converge to the origin in the fixed time $T < T_1 + T_2$, which is expressed as

$$T_1 = \frac{2^{\frac{2-\alpha}{2}}}{k_1(2-\alpha)} + \frac{2^{\frac{1-\beta}{2}}}{k_2(\beta-1)} \tag{39}$$

$$T_2 = T_A + T_B = \frac{2^{\frac{2-\alpha}{2}}}{a(2-\alpha)} + \frac{2^{\frac{1-\beta}{2}}}{b(\beta-1)} + \frac{1}{\widehat{a}} \ln\left(\frac{\widehat{a}\, l}{\widehat{b}} + 1\right) \tag{40}$$

where $T_1$ denotes the time costs for $\boldsymbol{s}$ to reach $\boldsymbol{s}(T_1) = \boldsymbol{0}$ from $\boldsymbol{s}(0)$. Then, on the sliding surface $\boldsymbol{s} = \boldsymbol{0}$, $T_2$ represents the time costs for $\boldsymbol{e}_1$ and $\boldsymbol{e}_2$ to reach $\boldsymbol{e}_1(T_1 + T_2) = \boldsymbol{0}$ and $\boldsymbol{e}_2(T_1 + T_2) = \boldsymbol{0}$ from $\boldsymbol{e}_1(T_1)$ and $\boldsymbol{e}_2(T_1)$.

*Proof:* To prove Theorem 2, we first select the following Lyapunov function candidate:

$$\begin{aligned}
V_1 = &\sum_{i=1}^{3}\left[\frac{1}{2}s_i^2 + \frac{1}{2\eta_{1i}}\left(\tilde{\boldsymbol{\omega}}_{fi}^T\tilde{\boldsymbol{\omega}}_{fi}\right) + \frac{1}{2\eta_{2i}}\left(\tilde{\boldsymbol{\omega}}_{ri1}^T\tilde{\boldsymbol{\omega}}_{ri1}\right)\right] \\
&+ \sum_{i=1}^{3}\left[\frac{1}{2\eta_{3i}}\left(\tilde{\boldsymbol{\omega}}_{ri2}^T\tilde{\boldsymbol{\omega}}_{ri2}\right) + \frac{1}{2\eta_{4i}}\left(\tilde{\boldsymbol{\omega}}_i^T\tilde{\boldsymbol{\omega}}_i\right)\right]
\end{aligned} \tag{41}$$

where $\eta_1 = \mathrm{diag}\{\eta_{11}, \eta_{12}, \eta_{13}\}$, $\eta_2 = \mathrm{diag}\{\eta_{21}, \eta_{22}, \eta_{23}\}$, $\eta_3 = \mathrm{diag}\{\eta_{31}, \eta_{32}, \eta_{33}\}$, and $\eta_4 = \mathrm{diag}\{\eta_{41}, \eta_{42}, \eta_{43}\}$ are positive-definite diagonal matrices. Then, taking the derivative of $\boldsymbol{s}$, we obtain that

$$\begin{aligned}
\dot{\boldsymbol{s}} = &\ \boldsymbol{D}\left(\boldsymbol{\theta}, \dot{\boldsymbol{\theta}}, \boldsymbol{u}\right) - \hat{\boldsymbol{D}} - k_1\mathbf{sig}^{\alpha-1}(\boldsymbol{s}) - k_2\mathbf{sig}^{\beta}(\boldsymbol{s}) \\
&- k_3\mathbf{tanh}(\boldsymbol{s}).
\end{aligned} \tag{42}$$

Afterwards, taking the derivative of (41) and inserting (42), we can derive that

$$\begin{aligned}
\dot{V}_1 = &\sum_{i=1}^{3}\left[-k_{1i}s_i\mathrm{sig}^{\alpha-1}(s_i) - k_{2i}s_i\mathrm{sig}^{\beta}(s_i) - k_{3i}s_i\tanh(s_i)\right] \\
&+ \sum_{i=1}^{3}\left[s_i\hat{\boldsymbol{\omega}}_i^T\left(\partial\hat{\boldsymbol{\phi}}_{\boldsymbol{\omega}_{fi}}\tilde{\boldsymbol{\omega}}_{fi} + \partial\hat{\boldsymbol{\phi}}_{\boldsymbol{\omega}_{ri1}}\tilde{\boldsymbol{\omega}}_{ri1} + \partial\hat{\boldsymbol{\phi}}_{\boldsymbol{\omega}_{ri2}}\tilde{\boldsymbol{\omega}}_{ri2}\right)\right] \\
&+ \sum_{i=1}^{3}\left[s_i\hat{\boldsymbol{\omega}}_i^T\boldsymbol{o}_i - s_i^2\left(F_{pi} + F_{vi}\right) + s_i\tilde{\boldsymbol{\omega}}_i^T\hat{\boldsymbol{\phi}}_i + s_i\delta_i\right] \\
&+ \sum_{i=1}^{3}\left[\frac{1}{\eta_{1i}}\left(\tilde{\boldsymbol{\omega}}_{fi}^T\dot{\tilde{\boldsymbol{\omega}}}_{fi}\right) + \frac{1}{\eta_{2i}}\left(\tilde{\boldsymbol{\omega}}_{ri1}^T\dot{\tilde{\boldsymbol{\omega}}}_{ri1}\right)\right] \\
&+ \sum_{i=1}^{3}\left[\frac{1}{\eta_{3i}}\left(\tilde{\boldsymbol{\omega}}_{ri2}^T\dot{\tilde{\boldsymbol{\omega}}}_{ri2}\right) + \frac{1}{\eta_{4i}}\left(\tilde{\boldsymbol{\omega}}_i^T\dot{\tilde{\boldsymbol{\omega}}}_i\right)\right].
\end{aligned} \tag{43}$$

Moreover, the weight update law is designed as

$$\begin{cases}
-\dot{\hat{\boldsymbol{\omega}}}_{fi}^T = \dot{\tilde{\boldsymbol{\omega}}}_{fi}^T = -\eta_{1i}s_i\hat{\boldsymbol{\omega}}_i^T\partial\hat{\boldsymbol{\phi}}_{\boldsymbol{\omega}_{fi}} \\
-\dot{\hat{\boldsymbol{\omega}}}_{ri1}^T = \dot{\tilde{\boldsymbol{\omega}}}_{ri1}^T = -\eta_{2i}s_i\hat{\boldsymbol{\omega}}_i^T\partial\hat{\boldsymbol{\phi}}_{\boldsymbol{\omega}_{ri1}} \\
-\dot{\hat{\boldsymbol{\omega}}}_{ri2}^T = \dot{\tilde{\boldsymbol{\omega}}}_{ri2}^T = -\eta_{3i}s_i\hat{\boldsymbol{\omega}}_i^T\partial\hat{\boldsymbol{\phi}}_{\boldsymbol{\omega}_{ri2}} \\
-\dot{\hat{\boldsymbol{\omega}}}_i^T = \dot{\tilde{\boldsymbol{\omega}}}_i^T = -\eta_{4i}s_i\hat{\boldsymbol{\phi}}_i^T.
\end{cases} \tag{44}$$

By inserting (44) into (43), we obtain that

$$\begin{aligned}
\dot{V}_1 = &\sum_{i=1}^{3}\left[-k_{1i}s_i\mathrm{sig}^{\alpha-1}(s_i) - k_{2i}s_i\mathrm{sig}^{\beta}(s_i) - k_{3i}s_i\tanh(s_i)\right] \\
&+ \sum_{i=1}^{3}\left[-s_i^2(F_{pi} + F_{vi}) + s_i\hat{\omega}_i^T o_i + s_i\delta_i\right]
\end{aligned} \tag{45}$$

where $k_{3i} \geq \Delta_0$. Then, we can deduce that

$$\dot{V}_1 \leq 0 \Rightarrow V_1(t) \leq V_1(0) \in \mathcal{L}_\infty \quad \forall t \geq 0. \tag{46}$$

Due to $\dot{V}_1 \leq -\boldsymbol{s}^T[\boldsymbol{s} \odot (\boldsymbol{F}_p + \boldsymbol{F}_v)]$, one can integrate both sides of $\dot{V}_1(t)$ to obtain that

$$\begin{aligned}
\Phi \triangleq &\int_0^t \boldsymbol{s}(\tau)^T\{\boldsymbol{s}(\tau) \odot [\boldsymbol{F}_p(\boldsymbol{\theta}(\tau)) + \boldsymbol{F}_v(\dot{\boldsymbol{\theta}}(\tau))]\}\mathrm{d}\tau \\
&\leq V_1(0) - V_1(t) \in \mathcal{L}_\infty,\ \forall t \geq 0
\end{aligned} \tag{47}$$

where (47) is valid in the two cases of $\boldsymbol{s}(\tau) = \boldsymbol{0}$ and $\boldsymbol{s}(\tau) \neq \boldsymbol{0}$ & $\boldsymbol{F}_p(\boldsymbol{\theta}(\tau)) + \boldsymbol{F}_v(\dot{\boldsymbol{\theta}}(\tau)) \in \mathcal{L}_\infty$.

*Case 1:* $\boldsymbol{s}(\tau) = \boldsymbol{0}$. The system reaches equilibrium when the sliding surface equals zero. In this case, both $\boldsymbol{\theta}$ and $\dot{\boldsymbol{\theta}}$ remain within their predefined boundaries, which ensures that all state constraints are satisfied.

*Case 2:* $\boldsymbol{s}(\tau) \neq \mathbf{0}$ & $\boldsymbol{F}_p(\boldsymbol{\theta}(\tau)) + \boldsymbol{F}_v(\dot{\boldsymbol{\theta}}(\tau)) \in \mathcal{L}_\infty$. If $\boldsymbol{\theta}$ or $\dot{\boldsymbol{\theta}}$ exceeds the predefined boundaries $(-\bar{\boldsymbol{\theta}}, \bar{\boldsymbol{\theta}})$ or $(-\bar{\boldsymbol{\theta}}_v, \bar{\boldsymbol{\theta}}_v)$, $\Phi$ will approach infinity, which violates (47). Hence, both $\boldsymbol{\theta}$ and $\dot{\boldsymbol{\theta}}$ remain within their predefined boundaries.

We will further prove the reachability of the sliding surface. For any initial state $\boldsymbol{\theta}(0)$ and $\dot{\boldsymbol{\theta}}(0)$, the proposed control method ensures that $\boldsymbol{\theta}$ and $\dot{\boldsymbol{\theta}}$ converge to the sliding surface $\boldsymbol{s} = \mathbf{0}$ in $T_1$. Another Lyapunov function candidate $V_2$ is designed as follows:

$$V_2 = \frac{1}{2}\boldsymbol{s}^T\boldsymbol{s}. \tag{48}$$

Afterwards, taking the derivative of (48) and inserting (42), we can derive that

$$\begin{aligned}\dot{V}_2 &= \sum_{i=1}^{3}\left[-k_{1i}s_i\mathrm{sig}^{\alpha-1}(s_i) - k_{2i}s_i\mathrm{sig}^{\beta}(s_i)\right] \\ &\quad + \sum_{i=1}^{3}\left[-k_{3i}s_i\tanh(s_i) + s_i\tilde{D}_i\right] \\ &\leq \sum_{i=1}^{3}\left[-k_{1i}s_i\mathrm{sig}^{\alpha-1}(s_i) - k_{2i}s_i\mathrm{sig}^{\beta}(s_i)\right] \\ &\leq \sum_{i=1}^{3}\left[-2^{\frac{\alpha}{2}}k_{1i}V_{2i}^{\frac{\alpha}{2}} - 2^{\frac{\beta+1}{2}}k_{2i}V_{2i}^{\frac{\beta+1}{2}}\right]\end{aligned} \tag{49}$$

where $k_{3i} \geq \Delta_0 \geq |\tilde{D}_i|$. According to Lemma 1, the convergence time $T_1$ is obtained, which is expressed as (39).

Finally, we will prove that the tracking errors $\boldsymbol{e}_1$ and $\boldsymbol{e}_2$ converge to the origin in $T_2$ on the sliding surface $\boldsymbol{s} = \mathbf{0}$. Due to $\boldsymbol{s}(t) = \mathbf{0}$ when $t > T_1$, based on (32), it is derived that

$$\begin{cases}\boldsymbol{e}_2 = -a\mathbf{sig}^{\alpha-1}(\boldsymbol{e}_1) - b\mathbf{sig}^{\beta}(\boldsymbol{e}_1), |e_{1i}| > l \\ \boldsymbol{e}_2 = -\widehat{a}\,\boldsymbol{e}_1 - \widehat{b}\,\mathbf{tanh}(\boldsymbol{e}_1), |e_{1i}| \leq l.\end{cases} \tag{50}$$

A Lyapunov function candidate $V_3$ is selected as

$$V_3 = \frac{1}{2}\boldsymbol{e}_1^T\boldsymbol{e}_1. \tag{51}$$

When $|e_{1i}| > l$, we can derive that

$$\begin{aligned}\dot{V}_3 &= -a\left(\boldsymbol{e}_1^T\boldsymbol{e}_1\right)^{\frac{\alpha}{2}} - b\left(\boldsymbol{e}_1^T\boldsymbol{e}_1\right)^{\frac{\beta+1}{2}} \\ &= -2^{\frac{\alpha}{2}}aV_2^{\frac{\alpha}{2}} - 2^{\frac{\beta+1}{2}}bV_2^{\frac{\beta+1}{2}}.\end{aligned} \tag{52}$$

According to Lemma 1, the tracking error $\boldsymbol{e}_1$ converges to a neighborhood near $l$ in the fixed time $T_A$, which can be expressed as follows:

$$T_A = \frac{2^{\frac{2-\alpha}{2}}}{a(2-\alpha)} + \frac{2^{\frac{1-\beta}{2}}}{b(\beta-1)}. \tag{53}$$

When $|e_{1i}| \leq l$, we can obtain that

$$\dot{V}_3 = -\widehat{a}\,\boldsymbol{e}_1^T\boldsymbol{e}_1 - \widehat{b}\,\boldsymbol{e}_1^T\mathbf{tanh}(\boldsymbol{e}_1) = -2\widehat{a}\,V_3 - \sqrt{2}\,\widehat{b}\,V_3^{\frac{1}{2}}. \tag{54}$$

Then, we can deduce that

$$\mathrm{d}t = \frac{1}{-2\widehat{a}\,V_3 - \sqrt{2}\,\widehat{b}\,V_3^{\frac{1}{2}}}\mathrm{d}V_3. \tag{55}$$

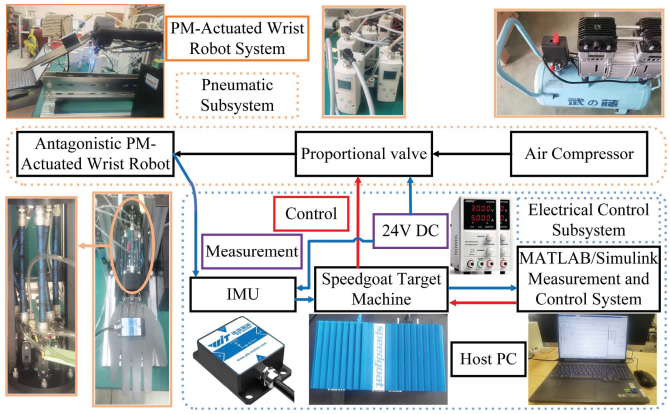


Fig. 4. Self-built experimental platform of antagonistic PM-actuated wrist robots.

By integrating both sides of (55), it is processed as follows:

$$\begin{aligned}T_B &= \int_0^{T_B} 1\mathrm{d}t = \int_{\frac{1}{2}l^2}^{0} \frac{1}{-2\widehat{a}\,V_3 - \sqrt{2}\,\widehat{b}\,V_3^{\frac{1}{2}}}\mathrm{d}V_3 \\ &= \int_0^{\frac{1}{2}l^2} \frac{1}{2\widehat{a}\,V_3 + \sqrt{2}\,\widehat{b}\,V_3^{\frac{1}{2}}}\mathrm{d}V_3.\end{aligned} \tag{56}$$

Let $\Theta = V_3^{\frac{1}{2}}$, we can derive that

$$\begin{aligned}T_B &= \int_0^{\frac{l}{\sqrt{2}}} \frac{1}{2\widehat{a}\,\Theta^2 + \sqrt{2}\,\widehat{b}\,\Theta}\mathrm{d}\Theta^2 \\ &= \int_0^{\frac{l}{\sqrt{2}}} \frac{2}{2\widehat{a}\,\Theta + \sqrt{2}\,\widehat{b}}\mathrm{d}\Theta \\ &= \frac{1}{\widehat{a}}\ln\left(\frac{\widehat{a}\,l}{\widehat{b}} + 1\right).\end{aligned} \tag{57}$$

Therefore, $\boldsymbol{e}_1$ will converge to the origin in the fixed time. According to the definition of (50), it is not difficult to obtain $\boldsymbol{e}_2 = \mathbf{0}$ when $\boldsymbol{e}_1 = \mathbf{0}$. In summary, when $t \geq T$, the tracking errors $\boldsymbol{e}_1$ and $\boldsymbol{e}_2$ converge to the origin. The proof process of Theorem 2 is accomplished.

## V. Experimental Validation

This section validates the proposed control method on a self-built antagonistic PM-actuated wrist robot.

### A. Self-Built Antagonistic PM-Actuated Wrist Robot

Fig. 4 exhibits the self-built experimental platform of the antagonistic PM-actuated wrist robots, comprising the pneumatic and electrical control subsystems.

The pneumatic subsystem includes 6 PMs (Festo DMSP-5-100N-RM-CM-DN, working pressure: 0–6 bar) and three sets of antagonistic joints. Two PMs control the movement of each antagonistic joint, with one acting as the agonist muscle and the other as the antagonistic muscle. The gas is generated by an air compressor (Wuteng 800W-80 L) and flows into the PMs through the proportional valves (Festo VPPM-6L-L-1-G18-0L6H-V1P-C1), forming a complete pneumatic circuit.

TABLE I
$e_{m1}, e_{m2}, t_{s1}, t_{s2}, \bar{e}_1, \bar{e}_2$, AND BAND ERRORS IN GROUP 1

| | $e_{m1}$ [deg] | $e_{m2}$ [deg] | $t_{s1}$ [s] | $t_{s2}$ [s] | $\bar{e}_1$ [deg] | $\bar{e}_2$ [deg] | Band errors of FE DOF [deg] | Band errors of AA DOF [deg] |
|---|---|---|---|---|---|---|---|---|
| The proposed method | **2.7** | **1.7** | **1.9** | **2.3** | **0.2** | **0.2** | **0.5** | **0.8** |
| The RBFNN-SMC method | 4.0 | 4.9 | 4.7 | 3.4 | 0.6 | 0.7 | 1.2 | 1.6 |
| The DO-ISMC method | 6.3 | 11.7 | 4.4 | 4.6 | 0.5 | 0.4 | 1.0 | 1.1 |

The bold values denote the optimal values.

TABLE II
$e_{m1}, e_{m2}, t_{s1}, t_{s2}, \bar{e}_1, \bar{e}_2$, AND BAND ERRORS IN GROUP 2

| | $e_{m1}$ [deg] | $e_{m2}$ [deg] | $t_{s1}$ [s] | $t_{s2}$ [s] | $\bar{e}_1$ [deg] | $\bar{e}_2$ [deg] | Band errors of FE DOF [deg] | Band errors of AA DOF [deg] |
|---|---|---|---|---|---|---|---|---|
| The proposed method | **2.6** | **0.9** | **2.1** | **1.7** | **0.2** | **0.2** | **0.4** | **0.7** |
| The RBFNN-SMC method | 3.8 | 5.4 | 4.6 | 3.4 | 0.6 | 0.7 | 1.3 | 1.6 |
| The DO-ISMC method | 4.0 | 5.9 | 4.3 | 5.0 | 0.6 | 0.5 | 0.8 | 0.7 |

The bold values denote the optimal values.

TABLE III
$e_{m1}, e_{m2}, t_{s1}, t_{s2}, \bar{e}_1, \bar{e}_2$, AND BAND ERRORS IN GROUP 3

| | $e_{m1}$ [deg] | $e_{m2}$ [deg] | $t_{s1}$ [s] | $t_{s2}$ [s] | $\bar{e}_1$ [deg] | $\bar{e}_2$ [deg] | Band errors of FE DOF [deg] | Band errors of AA DOF [deg] |
|---|---|---|---|---|---|---|---|---|
| The proposed method | **2.4** | **0.7** | **1.8** | **1.7** | **0.3** | **0.3** | **0.5** | **0.7** |
| The RBFNN-SMC method | 6.4 | 6.9 | 2.3 | 2.3 | 0.5 | 0.6 | 1.0 | 1.3 |
| The DO-ISMC method | 6.0 | 10.0 | 4.6 | 4.7 | 0.7 | 0.6 | 1.3 | 1.3 |

The bold values denote the optimal values.

In the electronic control subsystem, the integrated inertial measurement unit (IMU) installed on the end effector measures the joint angles and angular velocities of both the FE and AA DOF as feedback to the controller. The initial angle and angular velocity values are set to 0 deg. The baud rate is set to 115 200 and the accuracy of the IMU is 0.1 deg. Then, the Speedgoat real-time simulation and control system is utilized to transmit the feedback information of the IMU and control signals between the host PC and the experimental platform. The configuration of the host PC is equipped with an RTX 4060 GPU, 16 GB of memory, and an Intel Core i7 CPU. Meanwhile, the core control system runs in MATLAB/Simulink Real-Time Windows Target environment and calculates control input signals online, where the sampling time is set as 1 ms. The control input signals adjust the internal air pressure of PMs by controlling the valve opening of the proportional valves. Moreover, two direct current (DC) power supplies provide a stable 24 V supply to the IMU and proportional valves.

### B. Experimental Results and Analysis

This subsection validates the proposed method's effectiveness, robustness, and adaptability. To demonstrate its superiority, a RBFNN-based SMC (RBFNN-SMC) method [42] and a disturbance observer-based integral SMC (DO-ISMC) method [50] are used as comparative methods.[3]

Each group of experiments with the proposed method and comparative methods is repeated approximately 15 times to ensure the reliability and validate controller effectiveness. Each experimental group maintains the same experimental conditions, including the initial position of wrist robots, the initial air pressure of PMs, control gains, lumped disturbances, and desired trajectories. Furthermore, to provide a clearer visualization of the experimental results, a range of typical performance indicators and experimental results have been summarized in Tables I–III. The definitions of these indicators are outlined as follows.

1) $e_{m1}$ and $e_{m2}$ stand for the maximum angle tracking errors for the FE and AA DOF at $\forall\, t < 5$ s, respectively.
2) $t_{s1}$ and $t_{s2}$ denote the settling time for the FE and AA DOF, respectively. The error bands of the three groups of experiments are depicted in Tables I–III.
3) $\bar{e}_1$ and $\bar{e}_2$ represent the steady-state root-mean-square error (RMSE) for the FE and AA DOF, respectively. To maintain consistency, the RMSE is calculated for three groups of experiments starting from $t = 10$ s. The formula for calculating RMSE is represented as follows:

$$\bar{e}_i = \sqrt{\frac{1}{N}\sum_{k=1}^{N} e_{1i}(k)^2},\ i = 1, 2 \tag{58}$$

where $e_{1i}(k)$ represents the angle tracking error at the $k$th sampling period.

*1) Group 1: Irregular Trajectory Tracking-Validation of Feasibility:* In this group, sine functions are integrated with tanh-type functions to generate a series of irregular trajectories. The

[3]The comparative methods employ the RBFNN and DO, respectively, to estimate unmodeled dynamics, thereby validating the effectiveness of the proposed DLFNN. Meanwhile, the comparative methods design traditional SMC and ISMC, demonstrating that the proposed switching NTSMC method achieves smaller tracking errors, faster error convergence speed, and stronger robustness. Furthermore, the lack of error constraints in comparative methods may cause significant tracking errors in complex scenarios like human–robot interaction and substantial disturbances.

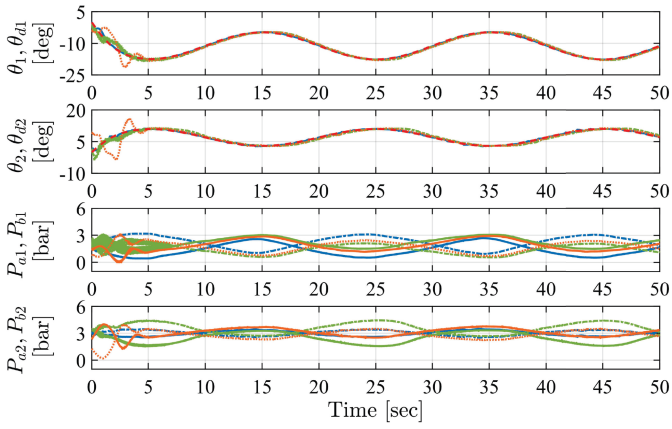


Fig. 5. Group 1: Control performance of irregular trajectories. The desired trajectories (red dashed lines), the proposed method (blue solid lines and dotted-dashed lines in the 3rd and 4th subplots), the RBFNN-SMC method (green dotted-dashed lines and solid lines in the 3rd and 4th subplots), and the DO-ISMC method (orange dotted lines and solid lines in the 3rd and 4th subplots).

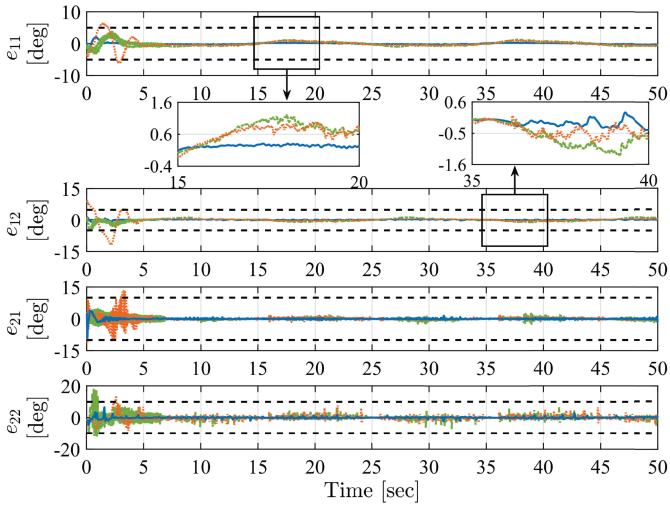


Fig. 6. Group 1: Tracking errors of irregular trajectories. The proposed method (blue solid lines), the RBFNN-SMC method (green dotted-dashed lines), the DO-ISMC method (orange dotted lines), and the error boundaries (black dashed lines).

specific expressions are given as follows:

$$\begin{cases} \theta_{d1} = -16\left[0.7\tanh(0.5t) + 0.4\sin\left(0.1\pi t\right)\right] \text{ deg} \\ \theta_{d2} = 10\left[0.7\tanh(0.5t) + 0.4\sin\left(0.1\pi t\right)\right] \text{ deg}. \end{cases}$$

For the proposed control method, the control parameters are specified as $k_p = 1 \times 10^{-2}$, $k_v = 1 \times 10^{-2}$, $\bar{\theta}_i = 5$, $\bar{\theta}_{vi} = 10$, $l = 0.2$, $a = 10^{-3}$, $b = 10^{-3}$, $\widehat{a} = 1.975 \times 10^{-3}$, $\widehat{b} = 1 \times 10^{-3}$, $\alpha = 1.5$, $\beta = 1.2$, $k_1 = \text{diag}\{2.8, 1\} \times 10^{-2}$, $k_2 = \text{diag}\{1, 1\} \times 10^{-3}$, $k_3 = \text{diag}\{1, 1\} \times 10^{-2}$, $\eta_1 = \text{diag}\{0.1, 0.1\}$, $\eta_2 = \text{diag}\{0.5, 0.5\}$, $\eta_3 = \text{diag}\{0.5, 0.5\}$, $\eta_4 = \text{diag}\{1, 1\}$, $\boldsymbol{c}_{11} = [-20, -16, -12, -8, -4, 0.1, 4, 8, 12, 16, 20]^T$, $\boldsymbol{c}_{12} = [-15, -12, -9, -6, -3, 0.1, 3, 6, 9, 12, 15]^T$, $\boldsymbol{c}_{21} = [-20, -16, -12, -8, -4, 0.1, 4, 8, 12, 16, 20]^T$, $\boldsymbol{c}_{22} = [-20, -16, -12, -8, -4, 0.1, 4, 8, 12, 16, 20]^T$, $b_{imk} = 10$, $b_{imj} = 10$ where $i = 1, 2$, $m = 1, 2$, $k = j = 1, \ldots, 11$, the initial air pressure $P_{01} = 2.4$ bar, $P_{02} = 3$ bar, and the initial values of all weights in the DLFNN are set to 0.1.

Moreover, after reasonable adjustment, the control parameters of the RBFNN-SMC method are set as $P = 5 \times 10^{-3}$, $K_s = 1 \times 10^{-2}$, $\varepsilon_n = 1.2 \times 10^{-2}$, $a_d = 8 \times 10^{-3}$, $L = 0.1$, $\delta = 10$, $c = 200$, and the number of neurons in the hidden layer is $m = 11$. Then, the control parameters of the DO-ISMC method are selected as $K = 0.01$, $d_m = 1.5 \times 10^{-3}$, and $P = 2 \times 10^{-3}$.

In Group 1, the robot hand's rotation in the FE and AA DOF is controlled by two sets of antagonistic PMs, ensuring it accurately tracks desired trajectories, which can be observed from Figs. 5–6. Compared with the RBFNN-SMC and DO-ISMC methods, the proposed method achieves better performance in tracking accuracy, convergence time, and overshoot. Specifically, the proposed method fulfills the RMSE of 0.2 deg in Table I, which is significantly lower than those of the other two methods. Additionally, the convergence in the fixed time is guaranteed by the proposed method with slight chattering. The settling time, i.e., 1.9 and 2.3 s, is shorter than that of the RBFNN-SMC and DO-ISMC methods, demonstrating better transient performance. Furthermore, the error bands for FE and AA DOF are minimized to 0.5 deg and 0.8 deg, respectively, further verifying superior positioning accuracy. Moreover, the overshoot of the proposed method, i.e., 2.7 deg and 1.7 deg, is the smallest compared with the other two methods. Meanwhile, the control inputs are smoother with fewer fluctuations, exhibiting improved stability under operating conditions and minimizing hardware wear.

*2) Group 2: Variable Amplitude Trajectory Tracking Under the Lumped Disturbances–Validation of Robustness:* The variable amplitude trajectories of the FE and AA DOF are selected as follows:

$$\begin{cases} \theta_{d1} = -16\mathrm{e}^{-0.01t}\left[0.7\tanh(0.5t) + 0.4\sin\left(0.1\pi t\right)\right] \text{ deg} \\ \theta_{d2} = 10\mathrm{e}^{-0.01t}\left[0.7\tanh(0.5t) + 0.4\sin\left(0.1\pi t\right)\right] \text{ deg}. \end{cases}$$

The external disturbances artificially exerted on the antagonistic PM-actuated wrist robots are set as follows:

$$\boldsymbol{d}_L = \begin{cases} 0.5\sin\left(0.1\pi t\right), \ t \in (41.5 \text{ s}, 42.5 \text{ s}) \\ 0.18 + 0.6\sin\left(0.2\pi t\right), \ \text{otherwise}. \end{cases}$$

Moreover, the control parameters of three methods are the same as those of Group 1. From Figs. 7–8, it is evident that the proposed method exhibits superior performance in trajectory tracking and anti-disturbance compared with the RBFNN-SMC and DO-ISMC methods. The proposed method drives the antagonistic joints to their desired trajectories in 2.1 and 1.7 s, which is faster than the RBFNN-SMC method, i.e., 4.6 and 3.4 s and the DO-ISMC method, i.e., 4.3 and 5.0 s, as depicted in Table II. Furthermore, the proposed control method constrains the tracking errors to 0.4 deg and 0.7 deg, which are smaller than those of the RBFNN-SMC method (i.e., 1.3 deg and 1.6 deg) and the DO-ISMC method (i.e., 0.8 deg and 0.7 deg).

When the external disturbances suddenly increase between 41.5 and 42.5 s, the proposed method enables the PMs to rapidly return to their desired trajectories in 1.0 and 0.5 s, which is quicker than the other two methods, respectively. The maximum deviations in the FE and AA DOF do not exceed 0.9 deg and 1.1 deg, respectively, which are significantly smaller than the

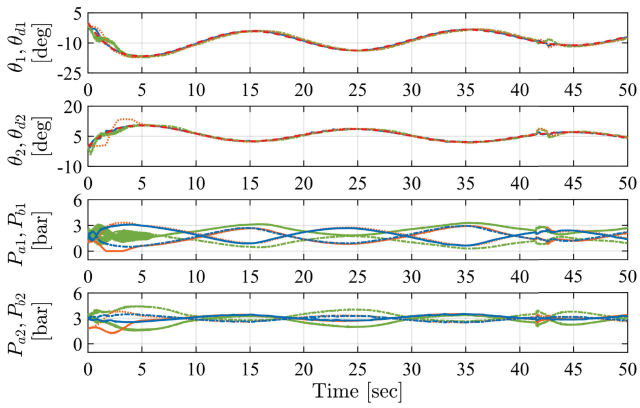


Fig. 7. Group 2: Control performance of variable amplitude trajectories under the lumped disturbances. The desired trajectories (red dashed lines), the proposed method (blue solid lines and dotted-dashed lines in the 3rd and 4th subplots), the RBFNN-SMC method (green dotted-dashed lines and solid lines in the 3rd and 4th subplots), and the DO-ISMC method (orange dotted lines and solid lines in the 3rd and 4th subplots).

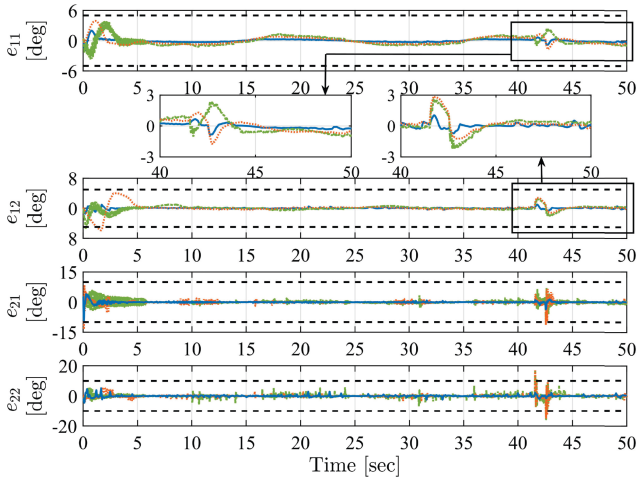


Fig. 8. Group 2: Tracking errors of variable amplitude trajectories under the lumped disturbances. The proposed method (blue solid lines), the RBFNN-SMC method (green dotted-dashed lines), the DO-ISMC method (orange dotted lines), and the error boundaries (black dashed lines).

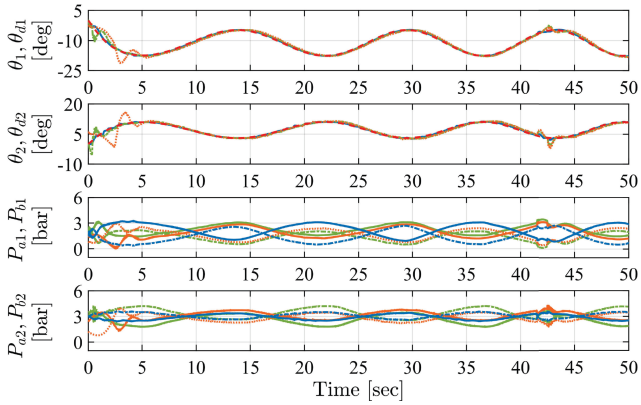


Fig. 9. Group 3: Control performance of variable frequency trajectories under the lumped disturbances. The desired trajectories (red dashed lines), the proposed method (blue solid lines and dotted-dashed lines in the 3rd and 4th subplots), the RBFNN-SMC method (green dotted-dashed lines and solid lines in the 3rd and 4th subplots), and the DO-ISMC method (orange dotted lines and solid lines in the 3rd and 4th subplots).

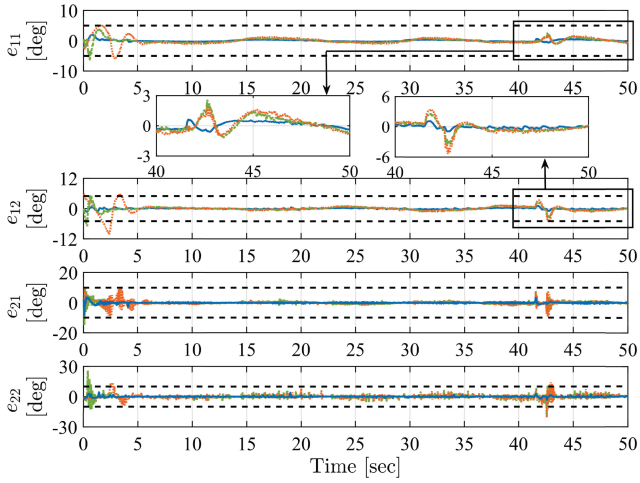


Fig. 10. Group 3: Tracking errors of variable frequency trajectories under the lumped disturbances. The proposed method (blue solid lines), the RBFNN-SMC method (green dotted-dashed lines), the DO-ISMC method (orange dotted lines), and the error boundaries (black dashed lines).

two comparative methods, validating the enhanced disturbance suppression of the proposed method.

*3) Group 3: Variable Frequency Trajectory Tracking Under the Lumped Disturbances–Validation of Adaptability:* To evaluate the adaptability of the proposed method, the selected trajectories with gradually increasing frequencies are specified as follows:

$$\begin{cases} \theta_{d1} = -16\left[0.7\tanh(0.5t) + 0.4\sin\left(0.1\pi t + 0.002t^2\right)\right] \text{ deg} \\ \theta_{d2} = 10\left[0.7\tanh(0.5t) + 0.4\sin\left(0.1\pi t + 0.002t^2\right)\right] \text{ deg}. \end{cases}$$

The control parameters of three methods are the same as those of Group 1. Moreover, the external disturbances exerted on the antagonistic PM-actuated wrist robots are the same as those in Group 2. From Figs. 9–10 and Table III, it can be seen that at both low and high frequencies, each joint angle can smoothly and accurately track the desired trajectory. The RMSE of the proposed control method is 0.3 deg, which is remarkably smaller than those of the RBFNN-SMC method (i.e., 0.5 deg and 0.6 deg) and the DO-ISMC method (i.e., 0.7 deg and 0.6 deg). Notably, the proposed control method exhibits satisfactory adaptability to multiple PMs under different frequency operating conditions. The PMs in the two comparative methods make it difficult to follow the rapid changes in the desired trajectory, leading to noticeable deviations and significant static errors. Moreover, while the RBFNN-SMC method appears to achieve fast convergence, this is mainly attributed to its large steady-state error, where the tracking errors continuously oscillate around the origin.

From the above three experimental groups, it can be concluded that the exponential constraint terms limit the joint angles and angular velocities within specific ranges without generating excessive control inputs. When the tracking errors of angles and angular velocities tend to exceed constraint boundaries, the proposed controller generates high-gain control signals to force the tracking errors back into the predefined safe ranges. The proposed control method demonstrates satisfactory control performance in all experiments, exhibiting excellent robustness

and adaptability. In contrast, the comparative methods exhibit constraint violations in most experiments, particularly during high-amplitude or high-frequency trajectory tracking.[4]

*Remark 1:* Increasing $k_p$ and $k_v$ ensures the tracking errors promptly converge to safe regions but may cause excessive control increments and unexpected chattering, degrading transient performance. Conversely, decreasing $k_p$ and $k_v$ provides smoother control inputs, but excessively small values degrade the ability to promptly correct constraint violations. Meanwhile, the predefined constraint ranges $\bar{\boldsymbol{\theta}}$ and $\bar{\boldsymbol{\theta}}_v$ depend on practical application requirements, safe operation of the end-effector, and workspace limitations of wrist robots. When setting $\bar{\boldsymbol{\theta}}$ and $\bar{\boldsymbol{\theta}}_v$, the contraction range and maximum input pressure of each antagonistic PM pair must be considered. Meanwhile, to prevent PMs over-contraction or over-extension caused by large tracking errors, reasonable $\bar{\boldsymbol{\theta}}$ and $\bar{\boldsymbol{\theta}}_v$ are selected to ensure stable operation of the wrist robots within their workspace. Notably, excessively small error constraint boundaries may cause system instability due to the inherent dynamic characteristics of PMs, resulting in system chattering while maintaining desired tracking performance.

*Remark 2:* It is shown from (32) that when $1 < \alpha < 2$, the control inputs in (33) tend to infinity as $e_{1i} \to 0,\ i = 1, 2$ without the switching boundary parameter $l$, leading to singularity. To address this issue, $l$ is designed to ensure that $\text{sig}^{\alpha-2}(e_{1i}) < l^{\alpha-2}$. Appropriately decreasing $l$ can accelerate error convergence. However, excessively small $l$ values cause frequent switching of control inputs caused by IMU accuracy, IMU noises, and PM dynamics, resulting in instability and chattering. Additionally, frequent switching increases computational load and accelerates hardware degradation. Through reasonable parameter adjustment, $l$ is selected as 0.2.

*Remark 3:* The desired trajectories and lumped disturbances are designed based on the actual workspace and application requirements of the antagonistic PM-actuated wrist robots. To ensure a smooth startup of the wrist robots and operation within the workspace, Group 1 designs an irregular trajectory combining sine and hyperbolic tangent functions. Furthermore, to verify the tracking performance of the wrist robots under different operating conditions, Group 2 and Group 3 employ variable-frequency and variable-amplitude trajectories, respectively. To validate the robustness of the proposed method, the system is subjected to periodic sinusoidal disturbances for most of the experimental time and abrupt disturbances at 41.5–42.5 s to simulate unexpected conditions.

## VI. Conclusion

For antagonistic PM-actuated wrist robots, this article had proposed a switching NTSMC method with a DLFNN to ensure accurate tracking of desired trajectories in the fixed time. In detail, the DLFNN was developed to realize online estimation of the lumped disturbances. Specifically, the DLFNN updated both inner-loop and outer-loop weights simultaneously, providing enhanced learning capability, improved dynamic response, and superior robustness. Based on the estimated value, a switching NTSMC was deployed to ensure the tracking of desired trajectories in the fixed time. Notably, the slow convergence and singularity issues were eliminated by switching functions. In the limited working space, the angle and angular velocity constraints of antagonistic joints were guaranteed theoretically and practically. The Lyapunov-based functions were selected to demonstrate the asymptotic stability of the origin in the fixed time. Also, the continuity and differentiability of the sliding surface function at the switching points were proven. Eventually, several groups of experiments in different situations were conducted to validate the performance superiority of the proposed method. Even so, the main limitation of the proposed method was the lack of compliant control for safe and efficient human–robot interaction. Future work will address constant force interaction by designing adaptive impedance/admittance control methods.

[4]Unlike traditional rigid robots, antagonistic PM-actuated wrist robots have more complex structures, more severe parameter uncertainties, and higher safety requirements. Meanwhile, coordinating antagonistic and agonist muscles to safely accomplish complex tasks remains challenging. Furthermore, while multiple pairs of antagonistic PMs enable more flexible motions, wrist robots exhibit stronger joint coupling and system uncertainties, further increasing control complexity. The proposed method can be applied to simpler and traditional robotic platforms. In the future, we will consider more different experimental scenarios to comprehensively validate the control performance of the proposed method.

## Acknowledgment

The authors would like to thank the Associate Editor and reviewers for their valuable comments, which have substantially improved the quality of this paper.

## References

[1] N. Li et al., "Bioinspired musculoskeletal model-based soft wrist exoskeleton for stroke rehabilitation," *J. Bionic Eng.*, vol. 17, no. 6, pp. 1163–1174, Nov. 2020.

[2] H. Zhang, J. Fan, Y. Qin, M. Tian, and J. Han, "Active neural network control for a wearable upper limb rehabilitation exoskeleton robot driven by pneumatic artificial muscles," *IEEE Trans. Neural Syst. Rehabil. Eng.*, vol. 32, pp. 2589–2597, 2024.

[3] J. Han, S. Yang, L. Xia, and Y.-H. Chen, "Deterministic adaptive robust control with a novel optimal gain design approach for a fuzzy 2-DOF lower limb exoskeleton robot system," *IEEE Trans. Fuzzy Syst.*, vol. 29, no. 8, pp. 2373–2387, Aug. 2021.

[4] H. Yang, X. Gao, Y. Chen, and L. Hao, "Hammerstein adaptive impedance controller for bionic wrist joint actuated by pneumatic muscles," *IEEE Access*, vol. 7, pp. 47–56, 2019.

[5] Q. Ai et al., "High-order model-free adaptive iterative learning control of pneumatic artificial muscle with enhanced convergence," *IEEE Trans. Ind. Electron.*, vol. 67, no. 11, pp. 9548–9559, Nov. 2020.

[6] T. Yang, Y. Chen, N. Sun, L. Liu, Y. Qin, and Y. Fang, "Learning-based error-constrained motion control for pneumatic artificial muscle-actuated exoskeleton robots with hardware experiments," *IEEE Trans. Autom. Sci. Eng.*, vol. 19, no. 4, pp. 3700–3711, Oct. 2022.

[7] H. Wang et al., "Grasping state analysis of multi-DOF soft manipulators based on multimodal sensing and deep spiking fuzzy network," *IEEE Trans. Fuzzy Syst.*, vol. 33, no. 8, pp. 2397–2410, Aug. 2025.

[8] Y. Liu, Y. Yang, Y. Peng, S. Zhong, N. Liu, and H. Pu, "A light soft manipulator with continuously controllable stiffness actuated by a thin McKibben pneumatic artificial muscle," *IEEE/ASME Trans. Mechatron.*, vol. 25, no. 4, pp. 1944–1952, Aug. 2020.

[9] C. V. Baysal, "Implementation of rehabilitation modalities using a low-cost PAM actuated robotic orthosis," *IEEE Access*, vol. 11, pp. 103601–103615, 2023.

[10] J. Jeong, I. B. Yasir, J. Han, C. H. Park, S.-K. Bok, and K.-U. Kyung, "Design of shape memory alloy-based soft wearable robot for assisting wrist motion," *Appl. Sci.*, vol. 9, no. 19, Sep. 2019, Art. no. 4025.

[11] K. Schäffer, Y. Ozkan-Aydin, and M. M. Coad, "Soft wrist exosuit actuated by fabric pneumatic artificial muscles," *IEEE Trans. Med. Robot. Bionics*, vol. 6, no. 2, pp. 718–732, May 2024.

[12] N. Sun, D. Liang, Y. Wu, Y. Chen, Y. Qin, and Y. Fang, "Adaptive control for pneumatic artificial muscle systems with parametric uncertainties and unidirectional input constraints," *IEEE Trans. Ind. Inform.*, vol. 16, no. 2, pp. 969–979, Feb. 2020.
[13] X. Zhang, N. Sun, G. Liu, T. Yang, and Y. Fang, "Hysteresis compensation-based intelligent control for pneumatic artificial muscle-driven humanoid robot manipulators with experiments verification," *IEEE Trans. Autom. Sci. Eng.*, vol. 21, no. 3, pp. 2538–2551, Jul. 2024.
[14] D. Liang, N. Sun, Y. Wu, Y. Chen, Y. Fang, and L. Liu, "Energy-based motion control for pneumatic artificial muscle actuated robots with experiments," *IEEE Trans. Ind. Electron.*, vol. 69, no. 7, pp. 7295–7306, Jul. 2022.
[15] Y. Cao et al., "Adaptive proxy-based robust control integrated with nonlinear disturbance observer for pneumatic muscle actuators," *IEEE/ASME Trans. Mechatron.*, vol. 25, no. 4, pp. 1756–1764, Aug. 2020.
[16] H. Aschemann and D. Schindele, "Sliding-mode control of a high-speed linear axis driven by pneumatic muscle actuators," *IEEE Trans. Ind. Electron.*, vol. 55, no. 11, pp. 3855–3864, Nov. 2008.
[17] C.-J. Lin, C.-R. Lin, S.-K. Yu, and C.-T. Chen, "Hysteresis modeling and tracking control for a dual pneumatic artificial muscle system using Prandtl-Ishlinskii model," *Mechatronics*, vol. 28, pp. 35–45, Jun. 2015.
[18] S. Xie, G. Ren, J. Xiong, and Y. Lu, "A trajectory tracking control of a robot actuated with pneumatic artificial muscles based on hysteresis compensation," *IEEE Access*, vol. 8, pp. 80964–80977, 2020.
[19] J. Cao, S. Q. Xie, and R. Das, "MIMO sliding mode controller for gait exoskeleton driven by pneumatic muscles," *IEEE Trans. Control Syst. Technol.*, vol. 26, no. 1, pp. 274–281, Jan. 2018.
[20] T. Yang, N. Sun, H. Chen, and Y. Fang, "Adaptive optimal motion control of uncertain underactuated mechatronic systems with actuator constraints," *IEEE/ASME Trans. Mechatron.*, vol. 28, no. 1, pp. 210–222, Feb. 2023.
[21] Y. Yuan, Y. Yu, and L. Guo, "Nonlinear active disturbance rejection control for the pneumatic muscle actuators with discrete-time measurements," *IEEE Trans. Ind. Electron.*, vol. 66, no. 3, pp. 2044–2053, Mar. 2019.
[22] N. Lokesh and M. K. Mishra, "Design of a decoupled sliding mode control for four-leg distribution static compensator," *IEEE Trans. Power Deliv.*, vol. 37, no. 6, pp. 5014–5024, Dec. 2022.
[23] A. Lenz, S. R. Anderson, A. G. Pipe, C. Melhuish, P. Dean, and J. Porrill, "Cerebellar-inspired adaptive control of a robot eye actuated by pneumatic artificial muscles," *IEEE Trans. Cybern.*, vol. 39, no. 6, pp. 1420–1433, Dec. 2009.
[24] Y. Lv, H. Zhang, Z. Wang, and H. Yan, "Distributed localization for multi-agent systems with random noise based on iterative learning," *IEEE Trans. Neural Netw. Learn. Syst.*, vol. 35, no. 1, pp. 952–960, Jan. 2024.
[25] C. Sun, X. Wu, H. Yang, H. Han, and D. Zhao, "Multimodal learning-based interval type-2 fuzzy neural network," *IEEE Trans. Fuzzy Syst.*, vol. 32, no. 11, pp. 6409–6423, Nov. 2024.
[26] T. Yang, N. Sun, and Y. Fang, "Neuroadaptive control for complicated underactuated systems with simultaneous output and velocity constraints exerted on both actuated and unactuated states," *IEEE Trans. Neural Netw. Learn. Syst.*, vol. 34, no. 8, pp. 4488–4498, Aug. 2023.
[27] C. Chen, J. Huang, D. Wu, and X. Tu, "Interval type-2 fuzzy disturbance observer-based T-S fuzzy control for a pneumatic flexible joint," *IEEE Trans. Ind. Electron.*, vol. 69, no. 6, pp. 5962–5972, Jun. 2022.
[28] X. Fan and T. Li, "Fuzzy switching sliding mode control of T-S fuzzy systems via an event-triggered strategy," *IEEE Trans. Fuzzy Syst.*, vol. 32, no. 11, pp. 6172–6184, Nov. 2024.
[29] Q. Liu et al., "Design and control of a reconfigurable upper limb rehabilitation exoskeleton with soft modular joints," *IEEE Access*, vol. 9, pp. 166815–166824, 2021.
[30] Y. Qin, H. Zhang, X. Wang, N. Sun, and J. Han, "Adaptive set-membership filter based discrete sliding mode control for pneumatic artificial muscle systems with hardware experiments," *IEEE Trans. Autom. Sci. Eng.*, vol. 21, no. 2, pp. 1682–1694, Apr. 2024.
[31] Y. Cao, J. Huang, and C. Xiong, "Single-layer learning-based predictive control with echo state network for pneumatic-muscle-actuators-driven exoskeleton," *IEEE Trans. Cogn. Dev. Syst.*, vol. 13, no. 1, pp. 80–90, Mar. 2021.
[32] S. Diao et al., "Prescribed-time adaptive fuzzy control for pneumatic artificial muscle-actuated parallel robots with input constraints," *IEEE Trans. Fuzzy Syst.*, vol. 32, no. 4, pp. 2039–2051, Apr. 2024.
[33] X. Guan, Z. He, M. Zhang, and H. Xia, "Filtering-error constrained angle tracking adaptive learning fuzzy control for pneumatic artificial muscle systems under nonzero initial errors," *IEEE Access*, vol. 10, pp. 41828–41838, 2022.
[34] C. Chen, Y. Cao, X. Chen, D. Wu, C. Xiong, and J. Huang, "A fused deep fuzzy neural network controller and its application to pneumatic flexible joint," *IEEE/ASME Trans. Mechatron.*, vol. 28, no. 6, pp. 3214–3225, Dec. 2023.
[35] X. Zhang, G. Liu, S. Diao, T. Yang, Y. Fang, and N. Sun, "Admittance-based output feedback fuzzy switching control for PAM-driven parallel robots via nonsingular terminal sliding mode," *IEEE Trans. Autom. Sci. Eng.*, vol. 22, pp. 14247–14259, 2025.
[36] Y. Lv, H. Yan, K. Rao, H. Zhang, and Y. Zhang, "Fixed-time distributed position estimation of multiagent systems based on local bearing measurement," *IEEE/ASME Trans. Mechatron.*, to be published, doi: 10.1109/TMECH.2025.3605527.
[37] J. Zhang, F. Xu, X. Liu, S. Gu, and H. Geng, "Fixed-time dynamic surface control for pneumatic manipulator system with unknown disturbances," *IEEE Robot. Autom. Lett.*, vol. 7, no. 4, pp. 10890–10897, Oct. 2022.
[38] Y. Lv, Z. Wu, H. Zhang, Z. Wang, and H. Yan, "Local-bearing-based prescribed-time distributed localization of multiagent systems with noisy measurement," *IEEE Trans. Ind. Inform.*, vol. 20, no. 7, pp. 9518–9526, Jul. 2024.
[39] S. K. Pandey, S. L. Patil, and S. B. Phadke, "Regulation of nonminimum phase DC-DC converters using integral sliding mode control combined with a disturbance observer," *IEEE Trans. Circuits Syst. II, Exp. Briefs*, vol. 65, no. 11, pp. 1649–1653, Nov. 2018.
[40] L. Yin, Z. Deng, B. Huo, and Y. Xia, "Finite-time synchronization for chaotic gyros systems with terminal sliding mode control," *IEEE Trans. Syst. Man Cybern. Syst.*, vol. 49, no. 6, pp. 1131–1140, Jun. 2019.
[41] H. Liang, Z. Du, T. Huang, and Y. Pan, "Neuroadaptive performance guaranteed control for multiagent systems with power integrators and unknown measurement sensitivity," *IEEE Trans. Neural Netw. Learn. Syst.*, vol. 34, no. 12, pp. 9771–9782, Dec. 2023.
[42] D. Kong, W. Wang, D. Guo, and Y. Shi, "RBF sliding mode control method for an upper limb rehabilitation exoskeleton based on intent recognition," *Appl. Sci.*, vol. 12, no. 10, 2022, Art. no. 4993.
[43] G. Zhang, J. Wang, P. Yang, and S. Guo, "Iterative learning sliding mode control for output-constrained upper-limb exoskeleton with non-repetitive tasks," *Appl. Math. Model.*, vol. 97, pp. 366–380, Sep. 2021.
[44] K. Qian, Z. Li, S. Chakrabarty, Z. Zhang, and S. Q. Xie, "Robust iterative learning control for pneumatic muscle with uncertainties and state constraints," *IEEE Trans. Ind. Electron.*, vol. 70, no. 2, pp. 1802–1810, Feb. 2023.
[45] D. Li, C. L. P. Chen, Y.-J. Liu, and S. Tong, "Neural network controller design for a class of nonlinear delayed systems with time-varying full-state constraints," *IEEE Trans. Neural Netw. Learn. Syst.*, vol. 30, no. 9, pp. 2625–2636, Sep. 2019.
[46] T. Yang, Y. Xu, Y. Fang, D. Navarro-Alarcon, S. Men, and N. Sun, "Accelerated gradient-based neuroadaptive synchronization control for antagonistic PAM robot hands with obstacle avoidance and motion constraints," *IEEE Trans. Med. Robot. Bionics*, vol. 7, no. 1, pp. 377–391, Feb. 2025.
[47] Y. Chen et al., "A neuroadaptive control method for pneumatic artificial muscle systems with hardware experiments," *Mech. Syst. Signal Process.*, vol. 146, no. 1, Jan. 2021, Art. no. 106976.
[48] J. Fei and Z. Feng, "Fractional-order finite-time super-twisting sliding mode control of micro gyroscope based on double-loop fuzzy neural network," *IEEE Trans. Syst. Man Cybern. Syst.*, vol. 51, no. 12, pp. 7692–7706, Dec. 2021.
[49] E. Moulay, V. Léchappé, E. Bernuau, and F. Plestan, "Robust fixed-time stability: Application to sliding-mode control," *IEEE Trans. Autom. Control*, vol. 67, no. 2, pp. 1061–1066, Feb. 2022.
[50] K. Lee, J. Cha, and S. Park, "Disturbance observer-based control to guarantee a sliding mode without sliding mode control," *IEEE Access*, vol. 11, pp. 95632–95638, 2023.

**Yuexuan Xu** received the B.S. degree in automation and the M.S. degree in control science and engineering from the Hebei University of Technology, Tianjin, China, in 2020 and 2023, respectively. He is currently working toward the dual Ph.D. degree in control science and engineering with the Institute of Robotics and Automatic Information Systems, Nankai University, Tianjin, and in mechanical engineering with The Hong Kong Polytechnic University, Kowloon, Hong Kong.

His research interests include the nonlinear control of pneumatic artificial muscle-actuated robots.

**Shuzhen Diao** (Graduate Student Member, IEEE) received the B.S. degree in mathematics and applied mathematics and the M.S. degree in systems science from Liaocheng University, Liaocheng, China, in 2019 and 2022, respectively. She is currently working toward the Ph.D. degree in artificial intelligence with the Institute of Robotics and Automatic Information Systems, Nankai University, Tianjin, China.

Her research interests include the nonlinear control of pneumatic artificial muscle-actuated robots.

**Tong Yang** (Member, IEEE) received the B.S. degree in automation and the Ph.D. degree in control science and engineering from Nankai University, Tianjin, China, in 2017 and 2022, respectively.

She is currently an Associate Professor with Nankai University and the Shenzhen Research Institute, Nankai University, Shenzhen, China. Her research interests include the nonlinear control of pneumatic artificial muscle-actuated robots and underactuated systems, including rotary cranes, offshore cranes, and tower cranes.

Dr. Yang serves as an Associate Editor (editorial board member) for *Measurement and Control* and *Transactions of the Institute of Measurement and Control*.

**Xinlin Zhang** received the B.S. degree in electrical engineering and automation from Beijing Forestry University, Beijing, China, in 2021. He is currently working toward the Ph.D. degree in control science and engineering, under the supervision of Prof. Ning Sun, with the Institute of Robotics and Automatic Information Systems, Nankai University, Tianjin, China.

His research interests include the modeling of hysteresis and nonlinear control of pneumatic artificial muscle-actuated robots.

Mr. Zhang received the *Excellent Presentation Award* of the 8th IEEJ International Workshop on Sensing, Actuation, Motion Control, and Optimization.

**Ming Li** received the B.S. degree in electronic information science and technology from Shandong University, Jinan, China, in 2007, the M.Sc. degree in communication engineering from Ulm University, Ulm, Germany, in 2009, and the Ph.D. degree in communication networks from the Hamburg University of Technology, Hamburg, Germany, in 2017.

He is currently the Vice General Manager and CTO with Shandong Inspur Database Technology Company, Ltd., Jinan. Before joining the Inspur Group, he worked as a Senior Engineer with Intel Corporation. He serves as an Executive Director of the China Industry-University-Research Institute Collaboration Association (CIUR) and is the Director of the Jinan Key Laboratory of Distributed Databases. His current research interests include HTAP cloud-native high-performance databases, Big Data analytics systems, and edge computing.

**Yakun Gao** received the B.S. degree in computer science and technology from Shandong University, Jinan, China, in 2008.

He is currently serving as the Executive Deputy General Manager of Inspur Smart Supply Chain Technology (Shandong) Company, Ltd., Jinan, and as a first-term expert committee member of the National Two-Way Integration Standardization Technical Committee (TC573) under the Ministry of Industry and Information Technology (MIIT). His current research interests include applying IoT and AI technologies in supply chain systems.

**David Navarro-Alarcon** (Senior Member, IEEE) received the Ph.D. degree in mechanical and automation engineering from The Chinese University of Hong Kong, Hong Kong, in 2014.

Since 2017, he has been with The Hong Kong Polytechnic University, where he is currently an Associate Professor with the Department of Mechanical Engineering. His current research interests include perceptual robotics and control systems.

Dr. Navarro-Alarcon currently serves as an Associate Editor of IEEE TRANSACTIONS ON ROBOTICS and a Technical Editor of IEEE/ASME TRANSACTIONS ON MECHATRONICS.

**Ning Sun** (Senior Member, IEEE) received the B.S. degree in measurement and control technology and instruments (with honors) from Wuhan University, Wuhan, China, in 2009, and the Ph.D. degree in control theory and control engineering (with honors) from Nankai University, Tianjin, China, in 2014.

He is currently a Professor with Nankai University, the Shenzhen Research Institute of Nankai University, Shenzhen, China, and the Shenzhen Loop Area Institute, Shenzhen. His research interests include intelligent control for mechatronic/robotic systems with an emphasis on (industrial) applications.

Dr. Sun received the *Machines* 2021 Young Investigator Award, the prestigious Japan Society for the Promotion of Science (JSPS) Postdoctoral Fellowship for Research in Japan (Standard) in 2018, the *International Journal of Control, Automation, and Systems* Best Associate Editor Award in 2023, IEEE TRANSACTIONS ON SYSTEMS, MAN, AND CYBERNETICS: SYSTEMS Outstanding Associate Editor in 2024, several journal/conference best/outstanding paper awards, etc. He serves as an Associate Editor/a Technical Editor for several journals, including IEEE TRANSACTIONS ON INDUSTRIAL ELECTRONICS, IEEE TRANSACTIONS ON INTELLIGENT TRANSPORTATION SYSTEMS, IEEE TRANSACTIONS ON SYSTEMS, MAN, AND CYBERNETICS: SYSTEMS, IEEE/ASME TRANSACTIONS ON MECHATRONICS, IEEE TRANSACTIONS ON AUTOMATION SCIENCE AND ENGINEERING.